Results in Optics 24 (2026) 101082

Contents lists available at ScienceDirect

Results in Optics

journal homepage: www.sciencedirect.com/journal/results-in-optics

Terahertz metamaterial-based perfect absorber biosensor with AI integration and multiband double-negative response for early non-melanoma skin cancer detection

Musa N. Hamza [a,*], Mohammad Alibakhshikenari [b,c,**], Bal Virdee [d], Renu Karthick Rajaguru Jayanthi [d], Sunil Lavadiya [e], Iftikhar ud Din [f], Bruno Sanches [g], Slawomir Koziel [h,i], Abinash Panda [j], Ali Farmani [k], Zinelabiddine Mezache [l], Zaid Ahmed Shamsan [m], Hassan Zakeri [n], Tran Huy Hung [o]

[a] Department of Physics, College of Science, University of Raparin, Sulaymaniyah 46012, Iraq
[b] LERO, the Research Ireland Centre for Software, College of Science and Engineering, School of Computer Science, University of Galway, H91 TK33 Galway, Ireland
[c] Department of Electrical and Electronics Engineering, Dogus University, 34775, Umraniye, Istanbul, Türkiye
[d] Center for Communications Technology, School of Computing and Digital Media, London Metropolitan University, 166-220 Holloway Road, London N7 8DB, UK
[e] Department of Information and Communication Technology, Marwadi University, Rajkot 360003, Gujarat, India.
[f] Telecommunication Engineering Department, University of Engineering and Technology, Mardan 23200, Pakistan.
[g] Department of Electronic Systems Engineering, Escola Politécnica da Universidade de São Paulo São Paulo, Brazil
[h] Engineering Optimization & Modeling Center, Reykjavik University, 102 Reykjavik, Iceland
[i] Faculty of Electronics, Telecommunications and Informatics, Gdansk University of Technology, 80-233 Gdansk, Poland
[j] Department of Electronics and Communication Engineering, CMR Institute of Technology, Bengaluru 560037, India
[k] Department of electronics engineering, Lorestan university, Iran
[l] Institute of Optics and Precision Mechanics, University of Ferhat Abbas Setif 1, Setif 19000, Algeria
[m] Department of Electrical Engineering, College of Engineering, Imam Mohammad Ibn Saud Islamic University (IMSIU), Riyadh 13432, Saudi Arabia
[n] Department of Electrical Engineering, Amirkabir University of Technology, 424 Hafez Ave, Tehran 15875-4413, Iran
[o] Faculty of Electrical and Electronic Engineering, PHENIKAA School of Engineering, PHENIKAA University, Hanoi 12116, Viet Nam

ARTICLE INFO

Keywords:
Terahertz biosensor
Metamaterial absorber
Double-negative metamaterials
Multiband resonance
Non-melanoma skin cancer
Similarity-based classification framework
Spectral classification
Microwave imaging

ABSTRACT

This paper presents a multiband terahertz metamaterial-based biosensor designed as a perfect absorber for the early detection of non-melanoma skin cancer. The proposed structure integrates a meticulously engineered multilayer architecture that achieves simultaneous negative permittivity, permeability, and refractive index (double-negative response) within the 0–5 THz range. Unlike conventional terahertz sensors that rely on one or two resonances, our design produces approximately twenty high-Q absorption peaks, with eleven exceeding 95%, four exceeding 97%, and two surpassing 99% absorption. These dense resonances enhance field localization and increase sensitivity to dielectric variations in biological tissue. Numerical simulation demonstrates a sensitivity of 629.95 THz/RIU and a figure of merit of 15,179.59 RIU^{-1}, significantly outperforming existing metamaterial biosensors. To further improve diagnostic capability, a broadband spectral-analysis framework is incorporated to analyze the full terahertz spectral response using Euclidean distance, mean squared error, and correlation metrics. The Spectral classification framework reliably distinguishes between healthy and cancerous tissue profiles, enabling an automated and robust detection. The biosensor's performance is further validated by incorporating it into a microwave imaging system, which provides spatial confirmation of cancerous tissue. These results establish the proposed device as a compact, high-resolution, and non-invasive platform for the early diagnosis of non-melanoma skin cancer.

* Corresponding author.
** Corresponding authors at: LERO, the Research Ireland Centre for Software, College of Science and Engineering, School of Computer Science, University of Galway, H91 TK33 Galway, Ireland.
E-mail addresses: musa.nuraden@uor.edu.krd (M.N. Hamza), mohammad.alibakhshikenari@universityofgalway.ie (M. Alibakhshikenari), b.virdee@londonmet.ac.uk (B. Virdee), r.rajagurujayanthi1@londonmet.ac.uk (R.K.R. Jayanthi), zashamsan@imamu.edu.sa (Z.A. Shamsan), h.zakeri@aut.ac.ir (H. Zakeri), hung.tranhuy@phenikaa-uni.edu.vn (T.H. Hung).

https://doi.org/10.1016/j.rio.2026.101082
Received 10 May 2026; Received in revised form 25 June 2026; Accepted 2 July 2026
Available online 3 July 2026
2666-9501/© 2026 The Authors. Published by Elsevier B.V. This is an open access article under the CC BY license (http://creativecommons.org/licenses/by/4.0/).

1. Introduction

Early detection of skin cancer, especially non-melanoma skin cancers (NMSC) such as basal cell carcinoma (BCC), is critical for effective treatment and improved patient outcomes. Traditional diagnostic methods, including biopsy and histopathological examination, are invasive and time consuming. Recent advances in terahertz (THz) technology and metamaterials have opened new avenues for non-invasive, label-free, real-time biosensing (Hamza and Islam, 2023; Parvin et al., 2021; Hamza et al., 2024a; Sharma et al., 2015; Sun et al., 2025; Zhang et al., 2024; Li et al., 2025a; Liu et al., 2025; Sharma et al., 2025; Teber, 2024; Tong et al., 2025; Zhang et al., 2025; Hu et al., 2025; Jiang et al., 2025; Li et al., 2025b; Wang et al., 2025a; Yin et al., 2025; Abose et al., 2025; Bani et al., 2025; Ferdous et al., 2025; Khandakar et al., 2025; Kundu et al., 2025; Lee et al., 2025; Miah et al., 2025; Naim et al., 2025; Sadeque et al., 2025; Vineetha et al., 2025).

Metamaterials are artificially structured media engineered to control electromagnetic (EM) responses beyond those of natural materials. They offer unprecedented control over permittivity and permeability, permitting the design of perfect absorbers in the THz band through independent tuning of electric and magnetic resonances (Hoque et al., 2025; Wekalao et al., 2025; Ahmed et al., 2025; Farooq et al., 2024; Han et al., 2025; Kazemi et al., 2024; Elalaouy et al., 2025; Wang et al., 2025b; Zheng et al., 2024; Khalil et al., 2025; Uddin et al., 2025). Early demonstrations showed that a metamaterial absorber operating near 1.3 THz could realize significant absorption with only a single unit cell in the propagation direction (Sharma et al., 2015; Hamza et al., 2024b; Hamza et al., 2025; Park et al., 2014).

Building on this foundation, recent efforts have adapted THz metamaterial sensors for biomedical applications. For example, flexible THz metamaterial biosensors have been developed for label-free detection of tumour biomarkers, achieving high bulk refractive index sensitivity of approximately 325 GHz/RIU and low detection limits for relevant biomarkers (Park et al., 2017; Asgari et al., 2020). Another study demonstrated a dual-band metamaterial perfect absorber operating at approximately 0.78 THz and 0.904 THz with absorption exceeding 99.5%, tailored to discriminate between healthy skin and non-melanoma skin cancer tissues through shifts in resonance characteristics (Chen et al., 2020; Azab et al., 2021; Yang and Lin, 2021; Li et al., 2021).

Recent advances have also focused on tunable and broadband terahertz metamaterial absorbers. Fu and Chen developed a dual narrowband terahertz absorber based on MoS_2 and $SrTiO_3$ that achieved absorption exceeding 99% at 0.25 THz and 1.30 THz while enabling independent tuning of absorption amplitude and resonance frequency through electrical and thermal control. In a related study, Yang et al. reported a graphene silicon heterostructure absorber that exploits the coupling of Mie, plasmonic, and Fabry Perot resonances to achieve broadband terahertz absorption and cancer cell detection. These studies demonstrate the growing potential of tunable and multiband terahertz metamaterial absorbers for sensing, modulation, and biomedical diagnostic applications (Fu and Chen, 2026; Yang et al., 2026).

More recently, a THz metasurface designed with electromagnetically induced transparency-like resonance on a flexible dielectric substrate was shown to distinguish normal keratinocytes from BCC cells with high sensitivity, achieving a theoretical sensitivity of approximately 550 GHz/RIU by tracking resonance frequency, transmission magnitude, and full width at half maximum (FWHM) variations. These advances illustrate the strong potential of THz metamaterials for early, non-invasive cancer diagnostics (Patel et al., 2022; Hoseini et al., 2022; Bhati and Malik, 2022; Hu et al., 2022; Tan et al., 2022; Shen et al., 2023).

However, existing metamaterial biosensors still face several limitations. Many sensors operate with a single or dual band response, which may restrict sensitivity and reduce the ability to discriminate subtle tissue variations. Structural designs often require compromises between high absorption performance and material tunability or robustness to variations in analyte properties such as thickness and refractive index (Mezache et al., 2023; Chen et al., 2023; El-Wasif et al., 2023; Nickpay et al., 2021). In addition, most reported systems rely solely on resonance shifts and amplitude variations without exploiting the full spectral information available from broadband sensor responses (Vafapour et al., 2021; Wang et al., 2021; Wang et al., 2020; Zhuang et al., 2022).

To address these limitations, we propose a THz metamaterial perfect absorber biosensor featuring multiband and double negative electromagnetic behavior, where both permittivity and permeability become negative over selected frequency regions (Wang et al., 2020; Zhuang et al., 2022; Asgari and Fabritius, 2023). The proposed design combines several advantageous characteristics:

1. Multiband response, enabling interrogation of tissue at multiple THz frequencies and improving detection robustness and selectivity.
2. Double negative metamaterial behavior, providing strong electromagnetic field confinement at the analyte interface and enhancing sensitivity to small changes in tissue dielectric properties such as refractive index, thickness, and hydration level.
3. Perfect absorber architecture, maximizing absorption efficiency while minimizing reflection and transmission losses, thereby improving detection contrast for subtle malignancy induced changes.
4. Broadband spectral classification, utilizing full spectral information rather than relying solely on individual resonance shifts, enabling improved discrimination between healthy and cancerous tissue states.

In this study, we present comprehensive computational modeling based on full wave electromagnetic simulations, together with sensitivity, quality factor, and figure of merit (FOM) analyses. A multiband double negative THz metamaterial perfect absorber is designed and optimized through systematic geometric and material parameter investigations. Absorption spectra and electromagnetic field distributions are analysed, and the sensing performance is evaluated using realistic tissue dielectric models representing healthy and non-melanoma cancerous skin tissues. The capability of the proposed biosensor to discriminate between different tissue states is investigated through variations in refractive index and analyte thickness. Furthermore, broadband spectral comparison techniques are employed to quantify spectral separation and classification performance. The proposed design is also compared with recently reported THz metamaterial biosensors, demonstrating competitive sensitivity, multiband operation, and enhanced sensing capability.

The convergence of metamaterial engineering, terahertz photonics, and advanced spectral analysis techniques represents a promising direction for next generation cancer diagnostics. The proposed device offers a non-invasive, label-free, rapid, and highly sensitive platform for early detection of non-melanoma skin cancer, potentially enabling point of care screening without the need for biopsy and thereby improving patient outcomes while reducing healthcare costs.

2. Modeling of the unit cell and electromagnetic evaluation

The proposed biosensor is based on a terahertz metamaterial perfect absorber (MPA) engineered to exhibit a stable and well-isolated multiband spectral response. To achieve this performance, a systematic modeling procedure was adopted, combining parametric geometry refinement, electromagnetic optimization, and sensitivity evaluation under simulated biologically relevant loading conditions. All numerical simulations were conducted in the frequency domain using a full-wave solver, applying proper periodic boundary conditions along the lateral directions and a normally incident plane wave excitation. The angle of incidence and polarization were also evaluated further to stress the design capabilities.

The metamaterial unit cell follows the classical three-layer absorber topology consisting of a patterned metallic resonator, a subwavelength

dielectric spacer, and a metallic ground plane. This configuration enables impedance matching to free space at multiple resonant frequencies while suppressing transmission, resulting in near-unity perfect absorption peaks, which are highly suited for biosensing applications.

2.1. Design methodology for the multiband terahertz biosensor

The development of the proposed multiband sensor architecture followed a structured multi-stage design methodology, illustrated in Fig. 1.

Each design stage was evaluated based on absorption efficiency, spectral separation between the resonant bands, quality factor, and field confinement characteristics, targeting the creation of a novel high performance biosensor proposal using a spiral incremental project management methodology.

The first iteration was based on a square split ring resonator and was widened, increasing the spaces between the metal parts. This introduced the base resonant geometry and served as a reference for evaluating mode formation mechanisms. Although this variant produced a set of dominant dipole resonances, the electric field localization and interband coupling were not fully sufficient to achieve the desired multiband characteristic.

The second design stage was planned to be used together with the first resonator, incorporating it inside it to activate higher-order resonant modes. This modification enabled the emergence of additional absorption peaks and improved spectral controllability. However, optimization was still required to maximize peak absorption and enhance sensitivity to dielectric perturbations.

The third configuration was the result of a complete change of strategy, focusing on the high side of the one THz spectrum. The structure used in this resonator was a novel mixture between a circular central ring and a set of three modified parts removed from an external centered ring.

The three sections detached from the ring were moved to the center, creating newer resonating modes and modified with respect to their endings. The sharpening applied to the endpoints increased the field localization and improved the frequency selectivity.

The final third design variant was the result of a multi-parameter optimization procedure involving resonator dimensions, gap widths, dielectric spacer thickness, and metal conductivity profiles. This variant successfully achieved several distinct absorption bands with high absorption magnitudes, robust angular stability, and enhanced near-field confinement properties essential for the biosensing functionality explored in later sections.

A comprehensive summary of the final structural and material parameters is provided in Table 1, ensuring reproducibility and facilitating comparison with related metamaterial absorber biosensors.

During the following parts of this work, the design variant 3 will be referred to as “Model 1” and the fully complete and optimized design unifying the three proposed variants will be referred to as “Model 2”, which is the final proposed design considered in this paper. The next section will address the tridimensional configuration of the absorber, and that will be followed by a deep analysis of its performance characteristics.

2.2. Excitation configuration and layered structure optimization

Fig. 2 illustrates the excitation configuration of the proposed terahertz (THz) metamaterial absorber, which is engineered to exhibit broadband absorption behavior spanning 0–5 THz. Because conventional electronic instrumentation is not capable of direct characterization above ~100 GHz, the experimental validation of the device relies on optical THz techniques such as THz time-domain spectroscopy (THz-TDS), laser-induced terahertz emission microscopy (LTEM), and thermal/pyroelectric sensing. These methods enable precise reconstruction of frequency-dependent absorption spectra and resonance characteristics across the full THz range.

The absorber consists of an aluminum-based resonant pattern deposited on a polyethylene terephthalate (PET) dielectric spacer. The resonator geometry incorporates both circular and square motifs, intentionally designed to excite coupled electric and magnetic resonant modes. When these modes coexist, the effective impedance of the absorber becomes nearly matched to free space, minimizing reflection while the ground plane suppresses transmission. This dual effect results in near-perfect absorption at the desired frequencies.

A plane wave with electric field E, magnetic field H, and propagation vector k impinges upon the structure at defined incidence (θ) and polarization (φ) angles. The angular and polarization dependence is crucial for evaluating the absorber's robustness, as practical sensing environments rarely guarantee perfect alignment.

Upon interaction with the resonant geometry, electromagnetic energy is guided into the lossy PET substrate, where it is dissipated as heat. This strong confinement not only achieves absorption levels

Table 1
Summary of Optimized Structural and Material Parameters Employed in the Finalized Metamaterial Biosensor Configuration.

Parameter	Value (μm)	Parameter	Value (μm)
A	141.42	J	20.339
B	68.185	K	113.13
C	28.21	L	50
D	48.86	M	56.56
E	14.14	N	150
F	39.36	O	36
G	54.54	PET thick (T_1)	10
H	31.49	Aluminum (Al) thick	0.2
I	35.22	Basal Cells thick (T3)	19
		Coverslip thick (T_2)	2

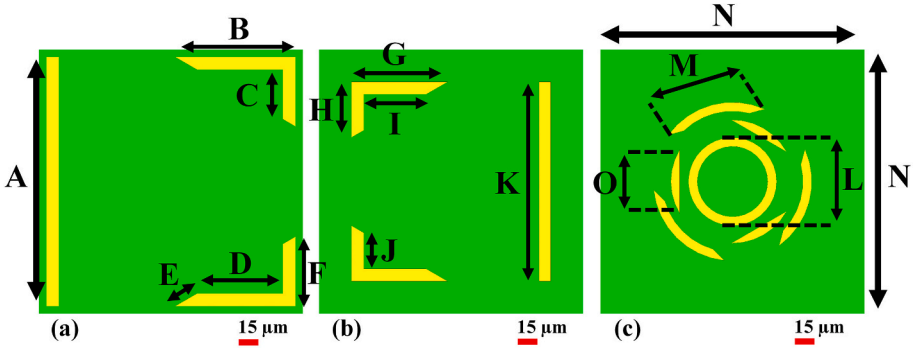


Fig. 1. Conceptual representation of the proposed metamaterial absorber integrating three design stages: (a) Initial prototype (Design Variant 1), (b) Intermediate configuration (Design Variant 2), and (c) Final optimized sensor architecture (Design Variant 3).

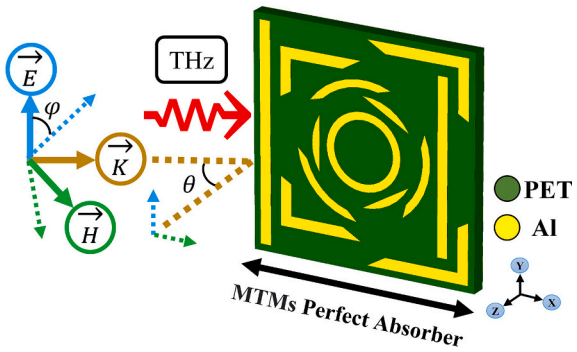


Fig. 2. Schematic depiction of the absorber arrangement showing the orientation of the incident terahertz wave relative to the stratified layer geometry.

approaching unity but also significantly amplifies near-field interactions with analyte layers—one of the key mechanisms enabling label-free biosensing, biochemical detection, and THz spectroscopic analysis.

Accurate simulation of micron-scale THz absorbers in CST Studio requires meticulous configuration of boundary conditions and excitation sources. Perfectly Matched Layers (PMLs) were used to eliminate artificial reflections and preserve the physical realism of the model. The computational domain was enlarged sufficiently beyond the metamaterial footprint to minimize near-field interaction with the boundaries, ensuring stable and accurate absorption calculations.

Mesh refinement was applied around geometrical discontinuities and subwavelength resonant features where strong gradients in the electromagnetic fields occur. This ensured accurate reconstruction of localized resonances and improved solution convergence, especially important for modeling high-frequency THz behaviors.

The excitation source was configured as a broadband, linearly polarized plane wave, enabling uniform activation of all relevant resonant modes. Symmetry planes, complex material dispersions, and detailed post-processing techniques were employed to extract absorption spectra, surface-current distributions, and electric-field profiles.

Through this deliberate integration of optimized boundary conditions, tailored excitation schemes, and rigorous numerical refinement, CST Studio provides physically meaningful simulations of the proposed micron-scale THz metamaterial absorber. This modeling framework forms the foundation for evaluating and demonstrating the biosensor's sensing behavior, which is elaborated in the subsequent sections.

3. Impact of structural and material parameters on absorptive performance

This section explores the metamaterial absorber's electromagnetic response by assessing how variations in geometry, constituent materials, and design topologies affect overall absorption efficiency. The evaluation includes S-parameters, refractive index, effective impedance, permittivity, and permeability to elucidate the underlying physical mechanisms that define sensor performance.

3.1. Comparative evaluation of design alternatives

In terahertz metamaterial perfect absorbers, the absorption mechanism is fundamentally determined by the relationship expressed in Eq. (1). The absorption, A, is defined as

$$A = 1 - R - T = 1 - |S_{11}|^2 - |S_{21}|^2 \quad (1)$$

where S_{11} and S_{21} denote the reflection and transmission coefficients, respectively. Because a metallic ground plane completely suppresses transmission ($T \approx 0$), the absorption simplifies to

$$A = 1 - R = 1 - |S_{11}|^2$$

Thus, the absorber's performance is ultimately governed by the minimization of reflection. Achieving this condition requires precise impedance matching between the metamaterial and free space ($Z_{abs} \approx Z_o$), allowing the incident terahertz wave to couple efficiently into the structure instead of being reflected.

When biological tissues, such as healthy skin layers or malignant skin cells, are placed atop the absorber, their distinct dielectric constants modify the overall impedance balance. This perturbation introduces measurable shifts in resonance frequency, absorption amplitude, and the depth of the reflection minima. These variations in $|S_{11}|$ form the basis for detecting pathology-associated dielectric differences, enabling highly sensitive identification of skin cancer using terahertz metamaterial absorber platforms.

Model 1 was selected as the baseline absorber structure consisting of a circular split ring resonator. To improve the number of resonant modes and enhance absorption performance, additional coupling elements were incorporated around the resonator, resulting in Model 2. These modifications increase electromagnetic field confinement and generate additional resonances across the THz spectrum, thereby improving the suitability of the structure for multiband biosensing applications. Fig. 3 illustrates the evolution from Model 1 to Model 2 and the corresponding changes in the absorption response.

To understand how resonator topology affects absorption behavior, two structural configurations, Model 1 and Model 2, are compared in Fig. 3. Because the ground plane ensures $T \approx 0$, every absorption peak in the spectrum corresponds to a frequency at which S_{11} is minimized and the electromagnetic field becomes strongly confined within the resonant elements.

Both designs exhibit multiple sharp absorption peaks, validating their multiband characteristics. These resonances originate from the intense near-field localization inside the metamaterial unit cell, an essential mechanism for biosensing, where even minute variations in analyte refractive index must lead to detectable spectral shifts.

Model 1 demonstrates a limited absorption window concentrated between 1.3 THz and 4.8 THz. In contrast, Model 2 exhibits a richer and more finely distributed set of resonances spanning 0.7–5 THz, with significantly sharper line shapes. The steeper resonance slopes improve the device's ability to discriminate subtle dielectric variations, making Model 2 a more robust platform for early-stage non-melanoma skin cancer detection, where small biochemical alterations must be identified with high precision.

3.2. Influence of material composition on electromagnetic behavior

The absorber's electromagnetic response is also highly sensitive to the intrinsic material properties of both the resonator and the substrate. Fig. 4(a) evaluates the effect of employing aluminum, silver, and gold as resonator materials across the 0–5 THz spectrum. Although all three metals exhibit plasmonic behavior, their conductivity profiles produce distinct absorption characteristics.

Silver, the most conductive, generates the strongest and narrowest absorption peaks due to its superior surface plasmon confinement. Gold, while slightly less conductive, provides chemically stable, consistently sharp resonances, beneficial for long-term biosensor deployment. Aluminum presents broader peaks because of its higher resistivity, which can be advantageous for broadband absorption requirements. These trends highlight the importance of resonator material selection in tailoring resonance amplitude, linewidth, and spectral uniformity in THz biosensing applications.

Fig. 4(b) examines the influence of substrate materials—including PET, Rogers RT5870, Polyimide, and Arlon AD410. Their differing dielectric constants and loss tangents cause shifts in resonance frequency and changes in absorption magnitude. Rogers RT5870, characterized by low dielectric loss, produces the sharpest and deepest resonances, enhancing sensitivity to small variations in biomolecular permittivity. PET and Polyimide lead to broader resonances due to higher losses,

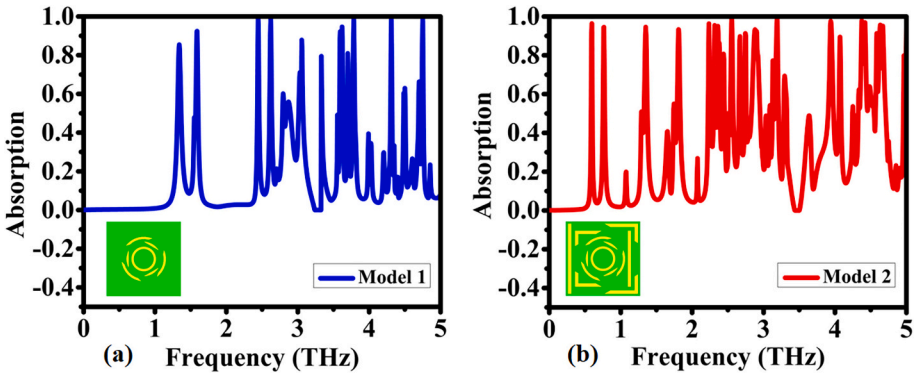


Fig. 3. Simulated absorption spectra of the proposed metamaterial absorber during the design evolution process: (a) Model 1 representing the initial resonator configuration and (b) Model 2 representing the optimized geometry. The comparison demonstrates the effect of the structural modifications on the resonance distribution, absorption characteristics, and multiband sensing performance of the proposed biosensor.

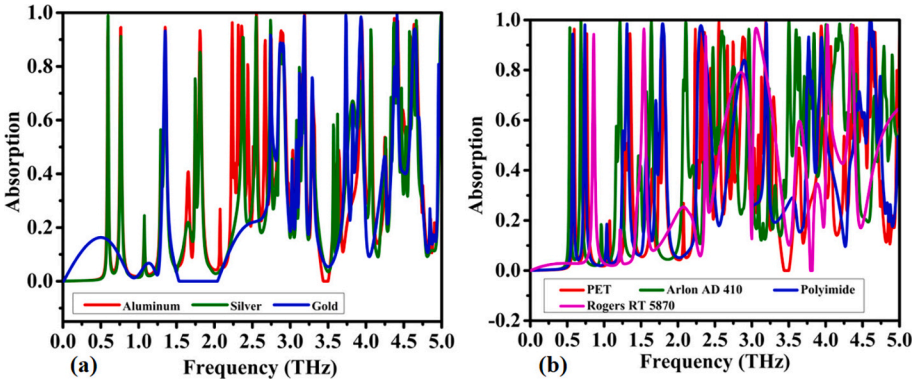


Fig. 4. Simulated absorption profiles showing (a) the influence of resonator materials and (b) variations due to substrate selection.

while Arlon AD410 provides a balanced mid-range performance suitable for stable integration. These findings confirm that substrate permittivity and loss strongly dictate field confinement and resonance quality.

Substrate thickness further modulates absorber behavior. As shown in Fig. 5(a), increasing the thickness from 10 μm to 40 μm shifts resonance frequencies and alters absorption amplitude. Thinner substrates confine fields more tightly at the resonator–substrate interface, producing stronger and more selective resonances. Thicker substrates introduce greater dielectric loading, broadening resonances, and slightly reducing peak absorption. This tunability allows designers to choose between high-Q narrowband sensing or broadband spectral monitoring depending on the application.

Fig. 5(b) compares reflection and absorption behavior across the operating band. The prominent dips in $|S_{11}|$ correlate directly with the absorption maxima, confirming efficient suppression of reflected energy and validating the impedance-matching behavior predicted by Eq. (1). The near-complementary nature of the reflection and absorption curves reinforces the absorber's operation as a metamaterial perfect absorber and demonstrates that both material composition and substrate geometry jointly determine the device's sensing precision.

3.3. Parameter-dependent electromagnetic analysis

The functional performance of the proposed metamaterial perfect absorber biosensor is fundamentally governed by its electromagnetic response under terahertz excitation. A rigorous evaluation of the

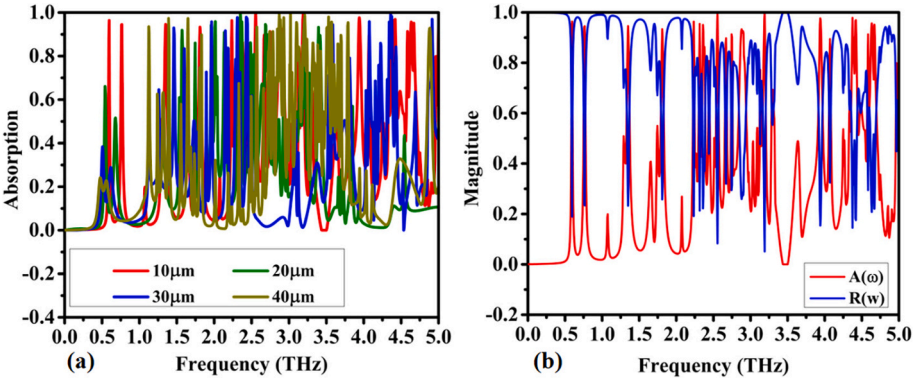


Fig. 5. Performance results demonstrating (a) the effect of substrate thickness on absorption magnitude and (b) comparative reflection and absorption characteristics across the operating frequency spectrum.

effective constitutive parameters is therefore essential to fully characterize the absorber's behavior and to explain the physical mechanisms responsible for its high absorption efficiency and sensing capability. These parameters include the frequency-dependent effective refractive index n(ω), permittivity ε(ω), permeability μ(ω), and wave impedance Z (ω), all of which collectively describe how the metamaterial interacts with incident electromagnetic waves.

To retrieve these effective parameters, analytical formulations based on the simulated scattering parameters, namely the reflection coefficient S_{11} and transmission coefficient S_{21}, are employed. The effective refractive index n(ω) is extracted using the standard S-parameter retrieval method and is expressed as

$$n(\omega) = \frac{1}{k_o d} cos^{-1}\left(\frac{1 - S_{11}^2 + S_{21}^2}{2S_{21}}\right) \quad (2)$$

where k_o denotes the free-space wave number and d represents the physical thickness of the metamaterial layer forming the absorber. This relation is particularly important for biosensing applications, as even a slight variation in the effective refractive index produces observable shifts in resonance frequency. Such shifts significantly enhance the sensor's sensitivity to minor dielectric perturbations introduced by biological analytes. Moreover, these high-fidelity spectral signatures serve as valuable inputs for AI-assisted inference models, which are trained to correlate resonance features with analyte concentration and composition, thereby enabling data-driven and highly reliable biosensing.

The effective permittivity is subsequently determined through the coupled interaction between the refractive index n(ω) and the wave impedance Z(ω). In biosensing environments, variations in permittivity directly influence the spatial distribution and intensity of the electric field near the resonator surface, making ε(ω) a critical parameter for detecting biochemical changes. Within the proposed AI-assisted framework, fluctuations in permittivity are exploited as discriminative spectral features for analyte classification. From a theoretical standpoint, effective permittivity is obtained using

$$\varepsilon(\omega) = n(\omega)/Z(\omega) \quad (3)$$

Magnetic permeability represents another essential parameter, as it governs the magnetic response of the metamaterial and strongly affects electromagnetic energy confinement and absorption performance. In metamaterial perfect absorbers, engineered magnetic resonances enable field localization that cannot be achieved using conventional materials. The effective permeability is calculated using

$$\mu(\omega) = Z(\omega)n(\omega) \quad (4)$$

Finally, the effective impedance Z(ω) acts as the unifying parameter that links permittivity and permeability and ultimately determines the absorber's ability to suppress reflection. Impedance matching between the metamaterial absorber and free space is a prerequisite for achieving near-perfect absorption at resonance. In the context of AI-assisted optimization and classification, impedance information provides an additional performance descriptor that allows the learning model to identify and refine resonator configurations yielding optimal absorption and enhanced sensing accuracy. The effective impedance is given by

$$Z(\omega) = \sqrt{\mu(\omega)/\varepsilon(\omega)} \quad (5)$$

The frequency-dependent scattering behavior of the proposed metamaterial absorber in the terahertz regime is illustrated in Fig. 6. Specifically, Fig. 6(a) presents the real and imaginary components of the reflection coefficient S_{11}, which exhibit pronounced oscillatory variations over the 0–5 THz frequency range. This oscillatory response reflects the strongly dispersive nature of the metamaterial and indicates the presence of multiple interacting resonant modes within the unit cell. Resonance conditions are identified at frequencies where the imaginary component approaches zero while the real component undergoes abrupt transitions. At these points, efficient coupling of the incident terahertz wave into the absorber occurs, leading to a significant reduction in reflected power and a corresponding enhancement in absorption.

Such oscillatory scattering behavior is a hallmark of metamaterial absorbers and originates from destructive interference between the incident electromagnetic wave and the re-radiated fields generated by induced electric and magnetic currents. This interference mechanism enables strong energy confinement within a subwavelength structure, thereby facilitating near-unity absorption.

Fig. 6(b) illustrates the corresponding frequency-dependent impedance response of the structure. At resonance frequencies, the real part of the normalized impedance approaches unity, while the imaginary part converges toward zero, indicating optimal impedance matching with free space. Under these conditions, the incident terahertz wave is efficiently coupled into the metamaterial, reflection is minimized, and electromagnetic energy is effectively trapped and dissipated within the structure. This impedance-matching condition constitutes the fundamental physical principle underlying perfect absorption in metamaterial-based devices.

Fig. 7 presents the retrieved effective electromagnetic parameters of the proposed metamaterial absorber across the 0–5 THz frequency range, providing deeper insight into its physical behavior. As shown in Fig. 7(a), the real part of the permittivity exhibits strong frequency dispersion, characterized by multiple inflection points associated with the excitation of distinct resonant modes. In contrast, the permeability demonstrates a pronounced resonance around 2.2 THz, where it undergoes a clear sign transition. This behavior indicates the presence of an engineered magnetic resonance induced by the metamaterial geometry, confirming the structure's capability to support strong magnetic field interactions alongside electric resonances.

Fig. 7(b) shows the corresponding imaginary components of ε and μ, which represent intrinsic loss mechanisms within the absorber. Sharp peaks in the imaginary part of the permeability align precisely with the resonance frequencies, confirming that absorption enhancement is driven by increased dissipative losses combined with strong electromagnetic field localization. Notably, the simultaneous occurrence of negative real values for both permittivity ($\varepsilon < 0$) and permeability ($\mu < 0$) indicate a double-negative electromagnetic response. In this regime, the metamaterial exhibits unconventional wave propagation characteristics, including backward-wave behavior, enabling enhanced control over electromagnetic energy confinement and propagation.

The retrieved effective parameters further reveal that the double-negative response occurs over finite frequency intervals surrounding several of the principal resonances rather than at isolated frequency points. These regions correspond to frequencies where both the real permittivity and real permeability simultaneously attain negative values. Importantly, the strongest absorption peaks observed in the absorption spectrum coincide with these double-negative regions, indicating that the simultaneous excitation of electric and magnetic resonances promotes impedance matching and enhanced electromagnetic field confinement. Consequently, the double-negative behavior contributes directly to the near-unity absorption characteristics and the high sensing performance of the proposed biosensor.

The combined behavior of the real and imaginary components validates that the absorber achieves high absorption efficiency through a balanced interplay between engineered dispersion and controlled loss mechanisms. These features are essential for ensuring high sensitivity, stability, and reproducibility in terahertz biosensing applications.

It should be noted that effective parameter retrieval in multiband metamaterial structures may be influenced by branch ambiguity and non-uniqueness, particularly in the vicinity of strong resonances. The extracted refractive index, permittivity, permeability, and impedance are therefore interpreted primarily as indicators of the underlying electromagnetic behavior and the occurrence of double negative characteristics. Although a rigorous Kramers Kronig consistency analysis is beyond the scope of the present work, the retrieved parameters exhibit physically reasonable trends that are consistent with the observed

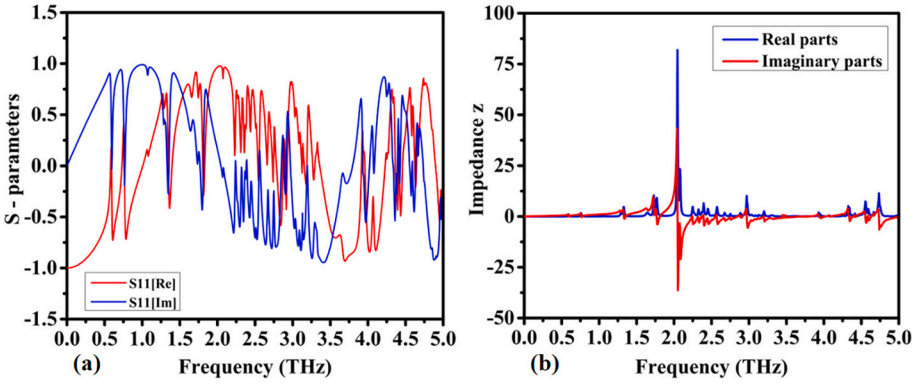


Fig. 6. S-Parameter and Impedance Characterization: (a) Real and imaginary components of the reflection coefficient (S_{11}), and (b) normalized impedance variation across the frequency spectrum.

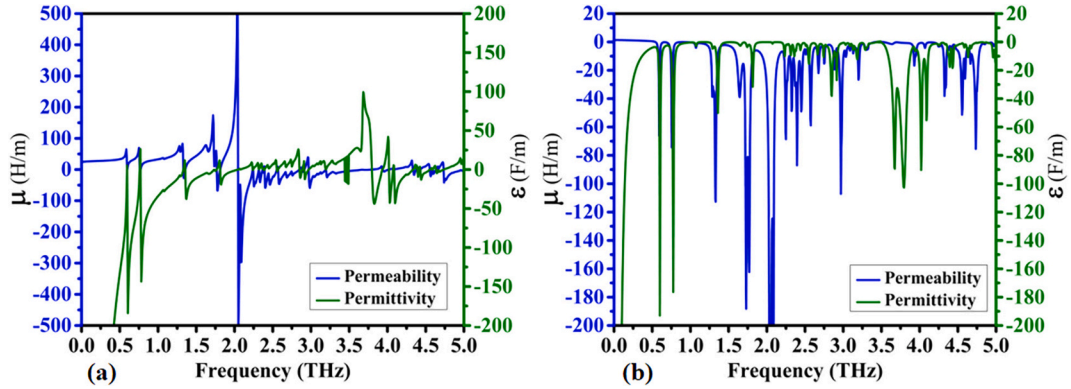


Fig. 7. Effective Electromagnetic Parameter Retrieval: (a) Real components of effective permittivity (ε) and permeability (μ), and (b) corresponding imaginary components.

absorption resonances and impedance matching behavior. Consequently, the extracted parameters are used here to provide qualitative physical insight into the resonance mechanisms governing the absorber performance.

3.4. Optical characteristics analysis

This subsection examines the optical characteristics of the proposed metamaterial absorber across the terahertz frequency range, with particular emphasis on their role in achieving near-unity absorption and high sensitivity. These parameters provide direct insight into resonance strength, reflection behavior, and dispersive properties, which collectively govern the device's performance.

Fig. 8(a) illustrates the frequency-dependent real and imaginary components of the effective refractive index. Strong dispersive behavior is observed in the vicinity of the resonance frequencies, where rapid variations occur in both components. These features arise from the simultaneous excitation of electric and magnetic resonant modes supported by engineered metamaterial geometry. From a sensing perspective, such dispersive regions are particularly important, as even minor perturbations in the surrounding dielectric environment, such as the presence of biomolecules, can induce measurable shifts in the refractive index, thereby modifying both the position and intensity of the resonances.

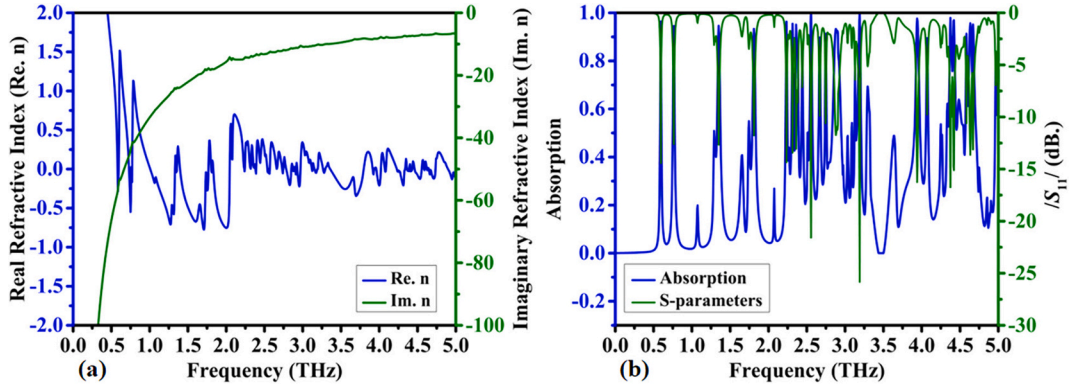


Fig. 8. Refractive Index and Reflection Analysis: (a) Real and imaginary components of the effective refractive index, and (b) reflection coefficient |S11| in decibels (dB).

Fig. 8(b) presents the reflection coefficient $|S_{11}|$ expressed in decibels. Deep minima in $|S_{11}|$ correspond directly to the absorption maxima, confirming that near-unity absorption is achieved through effective suppression of reflected energy. In practical biosensing applications, shifts in resonance frequency, variations in absorption amplitude, and changes in the depth of reflection minima serve as reliable indicators of analyte presence and concentration.

Importantly, the absorber demonstrates a multiband double-negative electromagnetic response, characterized by simultaneous negative permittivity and permeability across multiple frequency bands. This behavior enables the formation of several narrow and well-defined resonances, effectively providing multiple independent sensing channels within a single device. Such a multiband capability is highly advantageous for multiplexed biosensing, where different resonances can be utilized to detect multiple analytes or to improve detection reliability through cross-validation.

The optical analysis confirms that the proposed metamaterial absorber achieves strong field confinement and high spectral sensitivity, key requirements for robust and high-performance terahertz biosensing platforms.

4. Field distributions and surface current characteristics

This section provides an interpretation of the metamaterial's performance through spatial mapping of the electric and magnetic fields, as well as surface current densities at specific resonant modes. Such field-based analyses enable a clearer understanding of resonance localization, coupling mechanisms, and the sensor's optimization potential in the terahertz frequency regime.

4.1. Electric field intensity distribution

Fig. 9 illustrates the spatial distribution of the electric field magnitude over the resonator structure. The real component of $|E|$, shown in Fig. 9(a), reveals strong field localization near the central region of the half-circular periodic geometry, while comparatively weaker fields are observed toward the outer portions of the structure. This behavior indicates the formation of standing-wave patterns in the central region, where capacitive coupling across narrow gaps leads to intense electric-field enhancement. Such localization is a hallmark of effective electric resonance and plays a critical role in amplifying the interaction between the metamaterial surface and nearby biological analytes.

The imaginary component of the electric field, presented in Fig. 9(b), exhibits elevated intensity distributed across much of the resonator. This response reflects the presence of strong reactive fields associated with energy storage rather than radiation. The coexistence of inductive and capacitive effects at resonance indicates that the structure efficiently balances radiative coupling with localized energy confinement. Together, the real and imaginary field components demonstrate how electromagnetic energy is shared between propagating and stored modes, a condition that is essential for achieving strong absorption and enhanced sensitivity in metamaterial-based biosensors.

4.2. Magnetic field characteristics

The magnetic field distribution of the proposed design is depicted in Fig. 10, where both the real and imaginary components are examined to assess magnetic resonance behavior. In Fig. 10(a), the real part of $|H|$ exhibits pronounced localization in specific regions of the structure, corresponding to zones where circulating surface currents form closed loops. These localized magnetic hotspots are indicative of strong magnetic resonances, which are essential for achieving impedance matching and suppressing reflection in metamaterial perfect absorbers.

Fig. 10(b) shows the imaginary component of the magnetic field, which appears smoother and more uniformly distributed across the resonator. This behavior signifies stable reactive magnetic energy storage and reduced radiative loss at resonance. The combined real and imaginary magnetic field patterns confirm that the design supports well-defined and sustained magnetic resonances, contributing to the overall stability and robustness of the absorber's resonant modes.

4.3. Surface current mapping

Fig. 11 presents the simulated surface current distribution on the resonator, offering direct insight into the current pathways responsible for resonance excitation. The real component of the surface current, shown in Fig. 11(a), reveals strong conduction along the inner circular ring and adjacent slot regions, highlighted by regions of high current density. These areas define the primary electrical pathways that generate the dominant resonant modes. Irregular current patterns near the outer frame reflect geometric discontinuities that cause local redirection of current flow, further contributing to resonance formation through enhanced inductive and capacitive coupling.

The imaginary component of the surface current, illustrated in Fig. 11(b), displays a smoother and more symmetric distribution around the central resonator. The reduced current intensity toward the edges and the more uniform circulation around the inner geometry indicate significant reactive current storage, characteristic of inductive–capacitive resonance behavior. This balanced current distribution demonstrates the resonator's ability to sustain strong electromagnetic excitation without excessive radiation loss.

The combined analysis of electric and magnetic field distributions, together with surface current mapping, establishes a clear link between resonator geometry, field confinement, and resonance generation. These

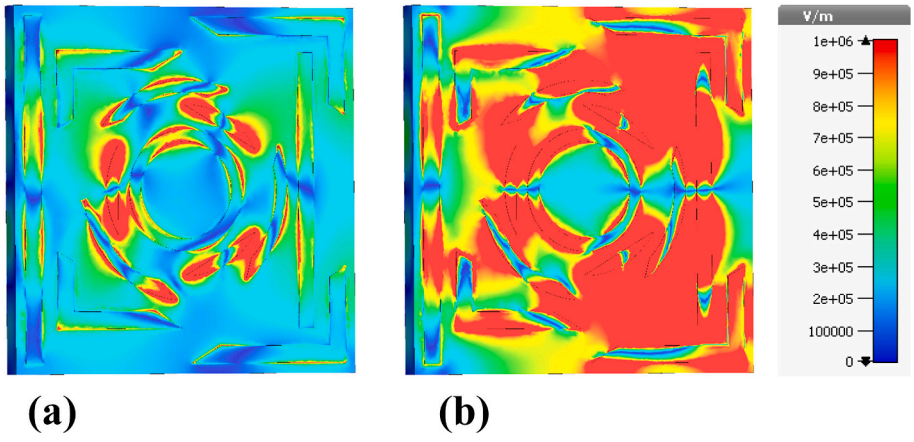


Fig. 9. Distribution of the electric field ($|E|$) across the resonator structure: (a) real field component, and (b) imaginary component.

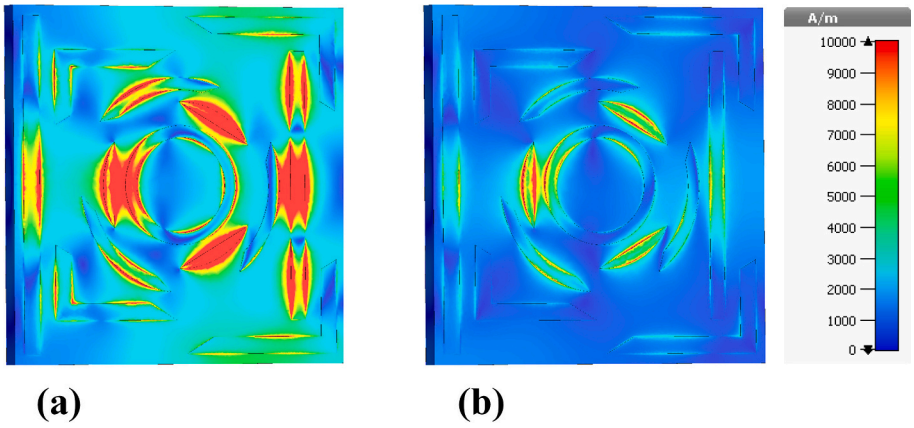


Fig. 10. Visualization of magnetic field (|H|) distribution within the metamaterial design: (a) real part, (b) imaginary part.

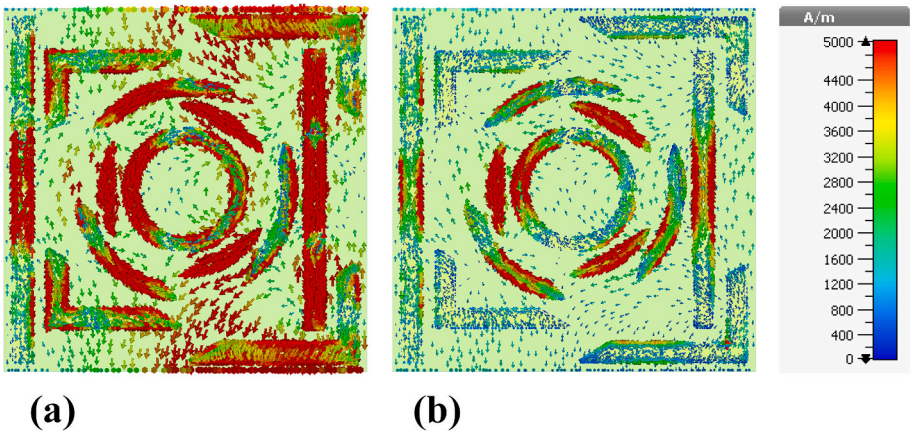


Fig. 11. Simulated surface current flow over the resonator structure: (a) real component, (b) imaginary component.

results confirm that the proposed metamaterial structure effectively concentrates electromagnetic energy at specific locations, enabling high absorption efficiency and enhanced interaction with the surrounding dielectric environment—key attributes for high-performance terahertz biosensing applications.

5. Application in non-melanoma skin Cancer diagnosis

Non-melanoma skin cancers (NMSC), including basal cell carcinoma (BCC) and squamous cell carcinoma (SCC), are characterized by measurable alterations in dielectric properties relative to healthy tissue. For the numerical simulations presented in this work, healthy skin tissue was modeled with a refractive index of approximately $n = 1.36$, whereas cancerous tissue was modeled with refractive indices in the range $n = 1.37$–1.38, corresponding to a dielectric contrast of approximately $\Delta n = 0.01$–0.02. These values were selected based on reported terahertz dielectric measurements in the literature, which consistently show increased refractive index and permittivity in malignant skin tissue due to elevated water content, increased cellular density, and structural changes associated with tumour development.

The proposed biosensor leverages these dielectric differences by monitoring changes in the absorption spectrum across multiple resonant peaks. Fig. 12 presents the absorption coefficient response of the sensor when exposed to healthy and cancerous skin models. Distinct variations are visible across multiple resonances, with cancerous tissue generating stronger localized absorption due to enhanced terahertz field coupling. These shifts arise from localized energy confinement at metasurface hotspots, making even small refractive deviations detectable.

To further validate diagnostic capability, Fig. 13 compares full-band spectral characteristics in the 0–5 THz range. Normal skin demonstrates stable resonance distributions with moderate absorption amplitudes, whereas cancerous tissue produces noticeable spectral deviations across multiple frequencies. This divergence is particularly pronounced at high-Q resonances, where the biosensor amplifies minor dielectric changes. The resulting multiband response produces a robust spectral signature unique to each tissue state, enabling classification without chemical markers or invasive sampling.

Beyond spectral contrast, spatial imaging provides an additional diagnostic dimension. In clinical practice, early-stage non-melanoma skin cancers may not exhibit clear visual symptoms, and conventional

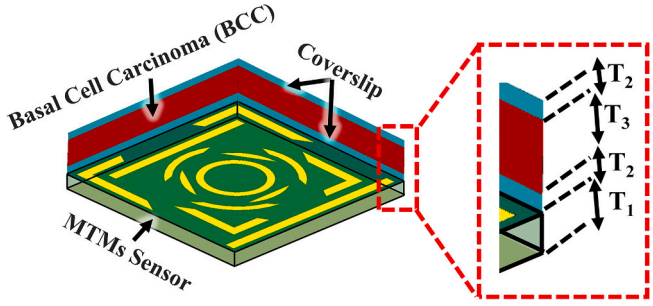


Fig. 12. Absorption coefficient response of the proposed biosensor for normal and non-melanoma cancerous skin samples.

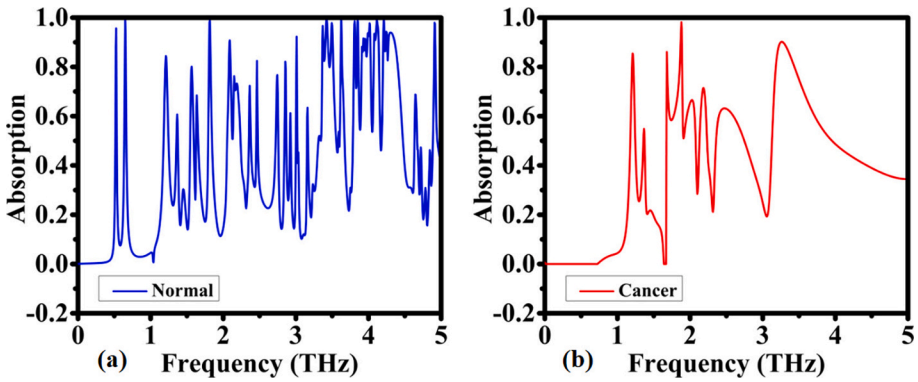


Fig. 13. Frequency-dependent absorption comparison over the 0–5 THz range for (a) normal skin tissue and (b) non-melanoma cancerous tissue.

terahertz reflectometry often fails to resolve subtle dielectric variations. To strengthen diagnostic reliability, the proposed framework integrates microwave imaging (MWI) as a complementary modality. Fig. 14 illustrates the sensing configuration, where the basal cell carcinoma tissue interacts with the metamaterial (MTM) sensor through a coverslip interface. In this arrangement, the MWI stage detects permittivity abnormalities in the region of interest, while the metamaterial absorber subsequently interrogates these localized anomalies through multiband terahertz resonances, providing electromagnetic confirmation and enabling tissue classification.

Field distributions extracted from imaging analysis reinforce this multimodal strategy. Under identical excitation, Fig. 15 reveals the electric field intensity associated with healthy and cancerous regions. The cancerous sample exhibits intensified field localization and stronger confinement near resonant interfaces, demonstrating enhanced energy absorption and dielectric perturbation. Complementary magnetic field results in Fig. 16 further show increased resonance-induced field coupling in malignant tissue. The stronger |H| distribution confirms that spectral deviations observed in Figs. 12 and 13 originate from fundamental resonance behavior, not background noise or numerical artifacts.

Taking together, these analyses establish a functional diagnostic pathway. Tissue is first screened through broadband absorption, producing multiresonant spectral fingerprints that distinguish healthy and malignant regions. Localized permittivity hotspots, consistent with early-stage NMSC, are then detected using microwave imaging, while the terahertz biosensor verifies malignancy through enhanced resonance shifts. This non-invasive diagnostic workflow enables both spatial localization and spectral classification, providing a dual-layer interpretive framework that is not achievable with single-modality terahertz biosensing.

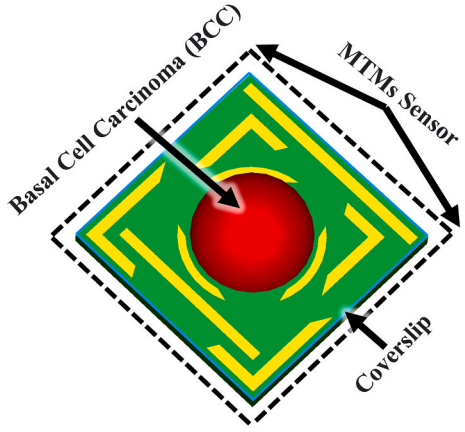


Fig. 14. Workflow diagram outlining the detection process for basal cell carcinoma (BCC) using microwave imaging (MWI).

6. Quantitative performance evaluation via broadband and AI-enhanced analysis

Having demonstrated the applicability of the proposed metamaterial absorber for non-melanoma skin cancer detection through dielectric contrast analysis, the next step is to evaluate its sensing performance quantitatively. Therefore, this section investigates key performance metrics, including quality factor, sensitivity, and figure of merit, which determine the capability of the proposed biosensor to discriminate between healthy and cancerous tissue states.

A rigorous quantitative assessment of the sensing capability was performed by evaluating the resonance sharpness, dielectric sensitivity, and discriminative accuracy between healthy and non-melanoma cancerous tissue. These metrics are derived from fundamental spectral properties and provide measurable indicators of diagnostic reliability.

The quality factor (Q) was employed to characterize the sharpness of each resonant absorption peak. As defined in eq. (6), the Q-factor is computed from the ratio of the resonant frequency f_0 *to the bandwidth* Δf *at half-power.*

$$Q_{factor} = \lambda / FWHM \tag{6}$$

High-Q resonances indicate low electromagnetic dissipation and strong field confinement, which are critical for biomedical discrimination. Owing to the multiband nature of the proposed absorber, individual resonances exhibit different linewidths and therefore different Q-factors. The reported value of $Q = 61.566$ represents the average quality factor calculated from the dominant resonances across the operating frequency range. While some resonances are broader and exhibit lower Q-factors, the sharper resonances demonstrate substantially higher values due to stronger electromagnetic field confinement and reduced radiation losses. Across the evaluated spectrum, the average Q-factor of 61.566 substantially exceeds values reported for many related terahertz metamaterial biosensors. *This strong resonance selectivity ensures that even minimal biological refractive index variations induce detectable spectral shifts.*

To quantify spectral sensitivity, the Euclidean sensitivity metric given in eq. (7) was applied to measure the cumulative deviation of absorption features between reference (healthy) and target (cancerous) samples.

$$S_{EUC} = \frac{\left\| A_{cancer} - A_{healthy} \right\|_2}{\Delta n} \tag{7}$$

The sensitivity calculation section has been revised to define the frequency range, spectral sampling basis, and physical meaning of the Euclidean sensitivity. The reported value of 629.95 THz/RIU corresponds to an integrated broadband sensitivity evaluated over the 0–5 THz frequency range rather than a conventional single-resonance frequency-shift sensitivity.

Unlike single-peak approaches, this metric captures broadband spectral dispersion, including both local and non-local resonance per-

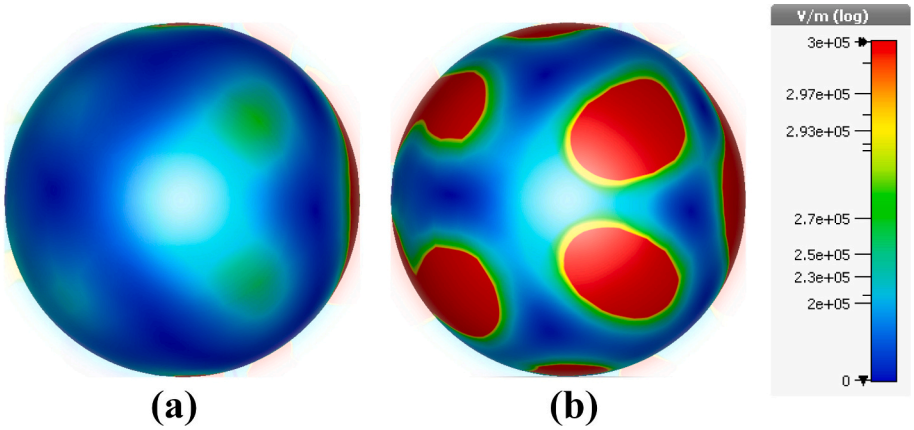


Fig. 15. Electric field intensity distribution derived from MWI: (a) healthy tissue, (b) cancerous non-melanoma skin tissue.

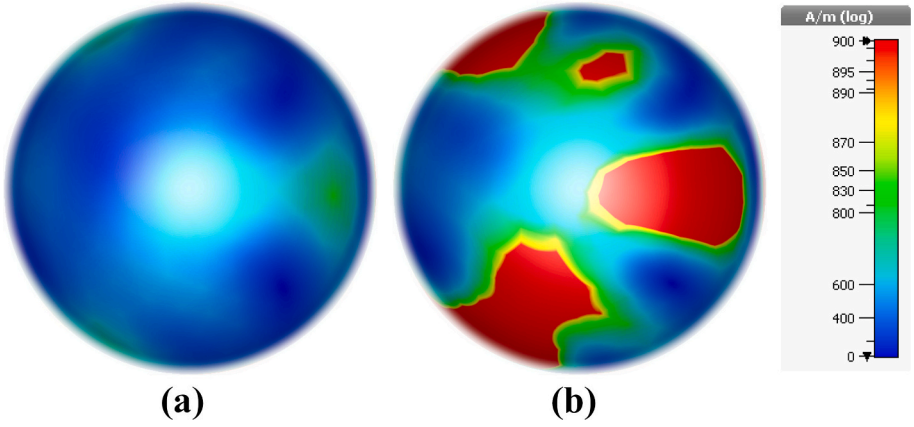


Fig. 16. Magnetic field imaging results demonstrating resonant field contrast for (a) normal and (b) cancerous tissue.

turbations. The Euclidean sensitivity was calculated using the complete absorption spectra of the healthy and cancerous tissue models over the 0–5 THz frequency range. The absorption responses were sampled at all frequency points generated by the full-wave electromagnetic simulation, and the Euclidean norm was evaluated across the entire spectral dataset. Consequently, the reported sensitivity does not represent a resonance shift $(\Delta f/\Delta n)$ associated with a single absorption peak. Instead, the calculated value of $S_{\mathrm{EUC}} = 629.95\mathrm{THz/RIU}$ quantifies the cumulative spectral separation between healthy and cancerous tissue states across the full operating band.

The AUC-based sensitivity in eq. (8) further evaluates the integrated deviation in absorption over the entire terahertz band.

$$S_{AUC} = \frac{|AUC_{cancer} - AUC_{healthy}|}{\Delta n} \tag{8}$$

This broadband approach avoids peak-locking and reduces false negatives arising from resonance drift, temperature variation, or biological noise. The AUC metric confirms that cancerous tissue consistently induces larger cumulative absorption energy than healthy tissue, demonstrating strong global response consistency across the 0–5 THz window.

To assess overall detection fidelity, the Figure of Merit (FOM) was employed as a measure of sensing performance. Because the proposed biosensor exhibits approximately twenty absorption resonances across the 0–5 THz operating band, the reported FOM was calculated using the Euclidean sensitivity and the average full-width at half-maximum (FWHM) of the dominant resonances. Owing to the multiband nature of the proposed absorber, the use of an average FWHM provides a representative broadband performance metric rather than one associated with a particular resonance. The FOM is therefore expressed as

$$FOM = \frac{S_{EUC}}{FWHM_{avg}} \tag{9}$$

The final biosensor achieves an exceptionally high FOM of 15,179.585 RIU^{-1}, far exceeding previous terahertz metamaterial platforms. Such a high FOM reflects the combined effects of narrow linewidth resonances, strong localized electromagnetic coupling, and distinct spectral separation between biological tissue states.

A comparative overview is presented in Table 2, which benchmarks the proposed device against existing terahertz biosensors. Earlier studies typically report sensitivities below 2 THz/RIU and Q-factors in the range of 5–15, with many devices relying on single- or dual-resonance mechanisms. In contrast, the presented design delivers high-density multiband absorption, approximately twenty distinguishable resonances, enabling superior sensitivity and resolution. This multiresonant behavior acts as a spectral fingerprint, significantly enhancing detection robustness, particularly for early-stage non-melanoma skin cancer where dielectric contrast is subtle.

These quantitative results confirm that the sensor's double-negative metamaterial architecture, strong electromagnetic localization, and broadband spectral evaluation enable precise tissue differentiation. The elevated Q-factor, Euclidean divergence, cumulative absorption contrast, and record-level FOM collectively position the proposed platform as a high-performance and clinically viable biosensing solution for early-stage cancer diagnostics.

From a practical implementation perspective, the proposed biosensor employs a relatively simple aluminum PET aluminum multilayer architecture that is compatible with established microfabrication technologies, including thin film deposition, photolithography, and micromachining processes commonly used in terahertz device

Table 2
Comparative summary of metamaterial-based biosensors reported in literature versus the proposed terahertz sensor.

Ref.	Year Published	FOM (RIU − 1)	Q	S (THz/RIU)	Bio-application
(Park et al., 2014)	2014	0.1216	5.58	0.02432	detection of Penicillia
(Park et al., 2017)	2017	–	–	0.0242, 0.02438	detection of Virus
(Asgari et al., 2020)	2020	–	–	0. 960	Biosensor, Collagen
(Chen et al., 2020)	2020	1.88	6.6	0.285	sensor
(Azab et al., 2021)	2021	–	10.64	1.65	Cancer detection
(Yang and Lin, 2021)	2021	–	–	0. 2833	Polystyrene particle
(Li et al., 2021)	2021	–	–	0.074	Cervical cancer
(Patel et al., 2022)	2022	3.86	13	0.207	Cancer detection
(Hoseini et al., 2022)	2022	0.166	–	1.06	detection of avian influenza virus
(Bhati and Malik, 2022)	2022	–	–	0.068	Hepatocellular carcinoma
(Hu et al., 2022)	2022	1.81, 1.57	8.21, 6.05	0. 203	sensor
(Tan et al., 2022)	2022	2.75	2.43	1.21	Cancer Diagnosis, Biosensor
(Shen et al., 2023)	2023	–	11	0.278	Bovine serum albumin protein
(Mezache et al., 2023)	2023	–	82	0.495	Cancer detection
(Hamza and Islam, 2023)	2023	0.86, 1.15	12.8, 13.5	0.0515, 0.076	Non-Melanoma Skin Cancer Diagnostics
This work	–	15,179.585	61.566	629.952804	Non-Melanoma Skin Cancer

fabrication. Realistic material properties, including finite metallic conductivity and dielectric losses of the PET substrate, were incorporated into the electromagnetic simulations. Although these losses influence resonance linewidth and absorption magnitude, they also contribute to the strong absorption characteristics required for sensing applications. Thermal noise, fabrication tolerances, and measurement uncertainties were not explicitly investigated in the present study. Nevertheless, the presence of multiple high-quality resonances, strong electromagnetic field localization, and significant broadband spectral separation between healthy and cancerous tissue responses is expected to improve robustness against practical measurement noise. Future work will focus on experimental validation, fabrication tolerance analysis, temperature-dependent measurements, and assessment of environmental noise effects under realistic operating conditions.

7. Broadband spectral classification of terahertz responses for Cancer detection

To enhance the diagnostic capability of the metamaterial biosensor, a machine learning (ML) framework is employed to interpret the broadband terahertz spectra. Instead of relying on isolated resonance peaks, the method evaluates the entire complex spectral response, capturing both amplitude and phase information associated with pathological tissue changes.

Step 1: Vector Construction

- $S_{11}^{real,h}$, $S_{11}^{imag,h}$: Real and imaginary S_{11} from healthy sample
- $S_{21}^{real,h}$, $S_{21}^{imag,h}$: Real and imaginary S21 from healthy sample
- $S_{11}^{real,c}$, $S_{11}^{imag,c}$: Real and imaginary S11 from cancer sample
- $S_{21}^{real,c}$, $S_{21}^{imag,c}$: Real and imaginary S21 from cancer sample

As shown in eqs. (10) and (11), the real and imaginary components of the reflection and transmission coefficients (S_{11}, S_{21}) from healthy and cancerous tissue samples are concatenated into feature vectors. Each vector contains $4N$ elements, where N corresponds to the number of sample frequency points. This representation preserves rich electromagnetic information, including resonance depth, shape, and phase variations that are highly sensitive to dielectric perturbations introduced by non-melanoma cancer tissue.

$$V_{healthy} = \left[S_{11}^{real,h}, S_{11}^{imag,h}, S_{21}^{real,h}, S_{21}^{imag,h}\right] \tag{10}$$

$$V_{cancer} = \left[S_{11}^{real,c}, S_{11}^{imag,c}, S_{21}^{real,c}, S_{21}^{imag,c}\right] \tag{11}$$

Step 2: Normalization.

To ensure consistency and numerical stability, all vectors are normalized using either *L2* normalization or *z*-score standardization as defined in eq. (12). Normalization suppresses uneven spectral amplitudes, equalizes contributions across frequency regions, and ensures that dominant peaks do not bias the model toward specific resonances.

$$\widehat{V} = \frac{V-\mu}{\sigma} \text{ or } \widehat{V} = \frac{V}{\|V\|_2} \tag{12}$$

Step 3: Pointwise Absolute Difference.

The frequency-wise absolute difference between the healthy and cancer spectral vectors is computed using eq. (13). This produces a differential signature that accentuates localized spectral perturbations and dampens frequency ranges where both tissue types exhibit similar responses. The resulting difference vector functions as a high-resolution contrast profile tailored to subtle dielectric variations.

$$D = \left|\widehat{V}_{cancer} - \widehat{V}_{healthy}\right| \tag{13}$$

Step 4: AI Score (Mean Difference).

The diagnostic score is calculated as the mean difference across the entire normalized feature space as expressed in eq. (14). Because the biosensor exhibits multiband absorption, each resonance contributes independently to this aggregated metric. A larger score indicates greater deviation from the healthy reference spectrum, reflecting stronger biological absorption and resonant perturbation typical of BCC tissue.

$$AI\ Score = \left(\frac{1}{4N}\right)\sum_{i=1}^{4N} Di \tag{14}$$

Step 5: Decision Rule.

Classification is performed using the threshold criterion in eq. (15). When the AI score exceeds the threshold T, the unknown sample is labeled as cancerous; otherwise, it is classified as healthy. The threshold is empirically tuned to maximize diagnostic accuracy and can be adapted to additional datasets or extended to other skin malignancies.

$$Prediction = \begin{cases} Cancer\ Detected, if\ AI\ Score > T \\ No\ Cancer, otherwise \end{cases} \tag{15}$$

The effectiveness of this ML-assisted scheme is illustrated in Fig. 17, where the spectral signatures of healthy and cancerous tissue are clearly separated. The model correctly identifies pathological tissue without requiring manual resonance tracking, handcrafted features, or prior assumptions about biological structure. Because the method incorporates the full broadband response, including both the real and imaginary characteristics of the metamaterial resonances, it remains robust against noise, peak drift, and environmental variability.

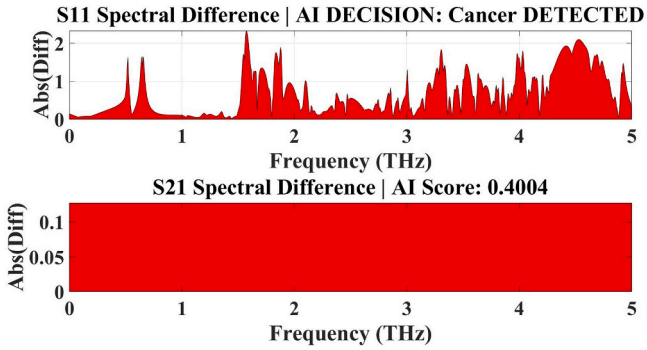


Fig. 17. Similarity-based classification framework–assisted classification of terahertz spectral signatures, highlighting diagnostic accuracy in distinguishing healthy and cancerous tissue.

8. AI-based diagnostic classification through spectral pattern recognition

While feature-based scoring provides an interpretable diagnostic signal, classifier performance improves substantially when spectral pattern similarity is considered. To achieve this, an AI-driven framework employing similarity metrics is applied to the complete absorption spectrum $A(f)$, eliminating the reliance on manually selected resonant peaks. Unlike the vectorized approach of Section 7, this method compares unknown spectra against established reference sets of healthy and cancerous tissue.

Note

- $f \in R^N$: frequency vector from 0.1 to 400 THz
- $A_u(f)$: absorption of the unknown sample
- $A_h^{(i)}(f)$: absorption of the i^{th} healthy sample
- $A_c^{(i)}(f)$: absorption of the i^{th} cancerous sample
- $\mu_h(f)$: mean spectrum of all healthy samples
- $\mu_c(f)$: mean spectrum of all cancerous samples

The first criterion is mean squared error (MSE), given in eqs. (16) and (17), which quantifies the average deviation of the unknown absorption response relative to the reference distributions. Lower MSE values indicate strong alignment with a particular spectral phenotype. Because cancerous tissue introduces multiple localized perturbations across the multiband absorption landscape, the MSE tends to increase significantly when compared to healthy references. This behavior reflects perturbation not only at dominant resonances, but also across adjacent spectral regions where the metamaterial exhibits subtle mode coupling.

$$MSE_h = \frac{1}{N}\sum_{j=1}^{N}\left[A_u(f_j) - \mu_h(f_j)\right]^2 \tag{16}$$

$$MSE_c = \frac{1}{N}\sum_{j=1}^{N}\left[A_u(f_j) - \mu_c(f_j)\right]^2 \tag{17}$$

The second metric is Euclidean distance, defined in eqs. (18) and (19). This measure captures cumulative deviation across all frequencies, emphasizing global spectral similarity rather than peak-specific differences. A cancerous spectrum typically produces a larger Euclidean distance due to broadband resonance intensification and enhanced absorption energy across the 0–5 THz range. This global sensitivity is particularly advantageous for early lesion detection, where localized dielectric deviations may be weak or distributed over smaller frequency windows.

$$EUC_h = \sqrt{\sum_{j=1}^{N}\left[A_u(f_j) - \mu_h(f_j)\right]^2} \tag{18}$$

$$EUC_c = \sqrt{\sum_{j=1}^{N}\left[A_u(f_j) - \mu_c(f_j)\right]^2} \tag{19}$$

To account for spectral morphology, the Pearson correlation coefficient, expressed in eq. (20), is applied. Pearson correlation evaluates spectral pattern alignment independent of absolute magnitude, enabling pattern-level differentiation even when amplitude differences are small. Healthy spectral responses generally show high cross-correlation due to consistent resonance positions and stable absorptive phase characteristics. Conversely, cancerous tissue disrupts resonant mode symmetry, leading to reduced correlation and clear pattern divergence.

$$r = \frac{\sum_{j=1}^{N}\left(A_u(f_j) - \widehat{A}_u\right)\left(\mu(f_j) - \widehat{\mu}\right)}{\sqrt{\sum_{j=1}^{N}\left(A_u(f_j) - \widehat{A}_u\right)^2 \sum_{j=1}^{N}\left(\mu(f_j) - \widehat{\mu}\right)^2}} \tag{20}$$

The effectiveness of these similarity-driven metrics is demonstrated in Fig. 18, where the test sample exhibits low MSE and short Euclidean distance relative to the healthy model, resulting in a correct "Healthy" classification. In contrast, Fig. 19 presents a spectrum with elevated energy and distorted resonance structure, generating a high Euclidean deviation and reduced pattern correlation, thus correctly categorized as "Cancerous." Importantly, this approach does not rely on any single peak or resonance frequency; instead, the classification emerges from collective spectral behavior across all modes.

These results confirm that spectral pattern recognition complements the physical sensitivity of the terahertz biosensor. By evaluating the full multiband absorption response and incorporating statistical measures of similarity, the AI-based classifier enhances diagnostic robustness, mitigates false positives, and allows consistent identification of early-stage non-melanoma skin cancer in heterogeneous biological samples.

$$Class = \begin{cases} \text{Cancerous if } \mathrm{MSE}_c < \mathrm{MSE}_h \text{ and } \mathrm{EUC}_c < \mathrm{EUC}_h \\ \textit{Healthy, otherwise} \end{cases} \tag{21}$$

9. Benchmarking

A comprehensive benchmarking exercise was performed to position the proposed biosensor within the current landscape of terahertz metamaterial sensors. The comparison encompasses structural configuration, electromagnetic performance, sensing capability, and biomedical diagnostic potential. As summarized in Table 3, most reported terahertz absorbers are designed for narrowband or dual-band operation and are primarily intended for the detection of specific biological analytes, refractive index variations, or individual disease markers. These devices typically rely on one or two resonant frequencies within a restricted spectral range. In contrast, the proposed biosensor exhibits a dense multiband absorption response extending across the 0–5 THz frequency range, with eleven resonances exceeding 95% absorption, four

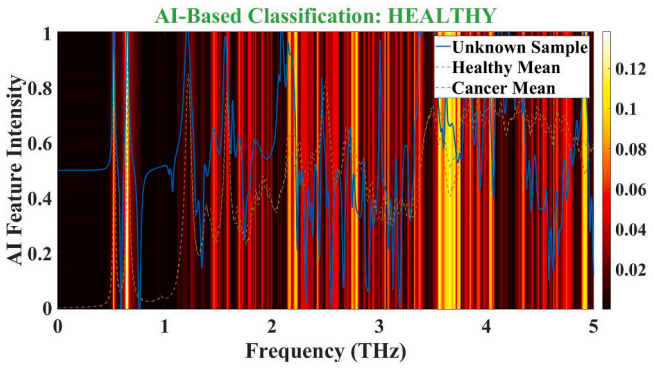


Fig. 18. Pattern correlation between test and reference spectra using mean squared error (MSE) and Euclidean distance—AI output: Healthy.

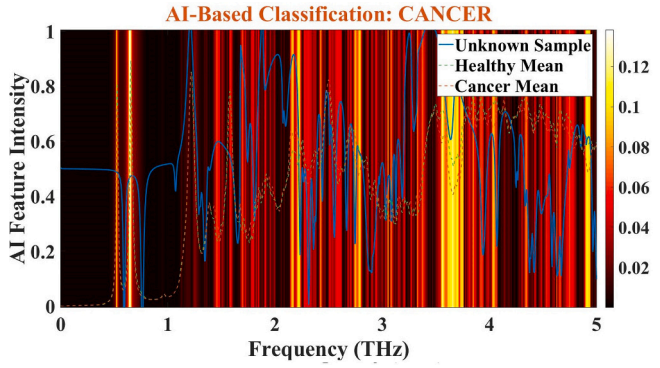


Fig. 19. Spectral feature comparison under identical analytical metrics—AI output: Cancerous.

exceeding 97%, and two approaching near unity absorption above 99%. The availability of multiple resonant modes provides broad spectral coverage and improves robustness against small dielectric variations associated with early-stage non-melanoma skin cancer.

The key design and performance innovations of the proposed biosensor are summarized in Table 4. Unlike conventional terahertz metamaterial absorbers that employ isolated resonators or limited resonance mechanisms, the proposed structure incorporates a hybrid resonator coupling scheme that generates spectral densification and supports approximately twenty resonant modes across the operating band. The engineered topology simultaneously exhibits negative permittivity, negative permeability, and negative refractive index characteristics within selected frequency regions, confirming the presence of double negative electromagnetic behavior. This response promotes enhanced electromagnetic energy confinement and stronger interaction between the resonant fields and biological tissue.

The absorber architecture is further optimized through careful selection of layer composition and geometric parameters to achieve effective impedance matching over the operating band. As a result, strong electric and magnetic field localization occurs at resonant hotspots throughout the structure, amplifying the interaction between the incident terahertz field and the biological sample. These characteristics contribute directly to the high sensing performance of the proposed biosensor.

From a sensing perspective, the proposed design achieves a Euclidean sensitivity of 629.95 THz/RIU, a figure of merit of 15,179.585 RIU^{-1}, and an average quality factor of 61.566 across the dominant resonances. The combination of high sensitivity, large figure of merit, and sharp resonance characteristics enables accurate discrimination between healthy and cancerous tissue states. Furthermore, the broadband multiresonance response reduces dependence on any single resonance and provides enhanced resilience to measurement uncertainty and tissue heterogeneity.

The benchmarking results presented in Tables 3 and 4 demonstrate that the proposed biosensor advances the state of the art through the combination of dense multiband absorption, double negative electromagnetic behavior, strong field localization, high sensitivity, high figure of merit, and high-quality factor. These attributes establish the proposed structure as a promising platform for non-invasive and label-free terahertz detection of non-melanoma skin cancer and other diseases characterized by subtle dielectric variations.

10. Future perspective

The presented terahertz metamaterial biosensor establishes a foundation for highly sensitive, label-free detection of non-melanoma skin cancer; however, several avenues remain open for further development. First, the current study is based on simulation-driven spectral responses and controlled dielectric models. Future work will focus on in vitro and ex vivo experimental validation, including terahertz measurements on excised skin samples and tissue-mimicking phantoms that capture microvascular, hydration, and collagen variations. Such validation will be essential to quantify biological variability and refine calibration procedures under realistic conditions.

A second direction involves miniaturization and hardware integration. While the multiband terahertz absorber demonstrates strong performance at the microscale, translating it into a portable diagnostic platform will require low-loss packaging, compact terahertz sources, and integrated readout electronics. Co-integration of microwave imaging and terahertz spectroscopy within a single probe could enable point-of-care scanning, complementing optical dermatoscopy and non-invasive dermatological tools.

Third, the embedded AI framework can be expanded toward adaptive and data-driven diagnostics. Current models use reference spectra and deterministic thresholds; future iterations may employ supervised training on large spectral datasets, continuous learning, or hybrid neural architectures that jointly process absorption, S-parameters, and spatial

Table 3
Comparative analysis between existing terahertz metamaterial absorbers and the proposed biosensing structure.

Ref.	Material substrate	Frequency operating THz	Absorptivity	Techniques used	Application
(Chen et al., 2023)	SiO_2	7–9.5	0.98	Au/SiO_2/ Graphene	Multi-Frequency Broadband and Ultra-Broadband
(El-Wasif et al., 2023)	silicon dioxide	1.5–1.7	0.972, 0.991	Gold/silicon dioxide/ Gold	biosensor for detecting coronaviruses
(Tan et al., 2022)	SiO_2	0.5–2.5	–	SiO_2/Graphene	Breast cancer detection
(Nickpay et al., 2021)	SiO_2	2–6	0.99	graphene/Au/SiO_2/Au	Refractive index sensor
(Vafapour et al., 2021)	Glass	0–0.37	0.998	Glass/InSb/MgF_2/InSb	Colon Cancer Detection
(Wang et al., 2021)	photonic crystal plate	1–3	0.97, 0.98, 0.99	bulk Dirac semimetal/ photonic crystal/Au	Narrowband perfect absorber
(Wang et al., 2020)	dielectric layer	1–3	0.99, 0.99	Au/dielectric layer/Au	Sensor
(Zhuang et al., 2022)	PET	0–3	0.99, 0.80, 0.95	PET/FSS/UV glue/ Graphene	Multifunctional Tunable Terahertz
(Asgari and Fabritius, 2023)	Teflon	0.7–5	>0.96	Ion gel/Graphene/Teflon/ Gold	polarization-sensitive
(Liu et al., 2020)	Topas spacer	0.5–4.5	0.99, 0.98, 0.99	graphene/Topas/Au	Ultra-Broadband Absorber
(Saadeldin et al., 2019)	dielectric Teflon	1–2.2	0.99	Au/dielectric Teflon/Au	Sensor
This work	PET	0–5	Eleven peaks: >0.95 Four peaks: >0.97 Two peaks: >0.99	Al/ PET /Al	Non-Melanoma Skin Cancer, Microwave Imaging, and Biosensor

Table 4
Design and Performance Innovations of the Proposed Biosensor.

Novelty Aspect	Scientific Description	Justification and Impact
Micron Scale Perfect Absorber Architecture	The biosensor utilizes a meticulously engineered metamaterial absorber structure in the micron scale, optimized to achieve near unity absorption across multiple resonances.	Miniaturization ensures compactness, high surface field confinement, and enhanced coupling efficiency for terahertz bio interactions.
Simultaneous Negative ε, μ, and n	The designed resonant topology achieves concurrent negative permittivity, permeability, and refractive index within the 0–5 THz regime.	The double negative response promotes backward wave propagation, enhanced energy localization, and stronger interaction with biological tissues.
Multiband Resonance Mechanism	The sensor exhibits approximately twenty resonances, including eleven peaks exceeding 95% absorption, four peaks exceeding 97%, and two peaks exceeding 99% absorption.	Multiple resonances provide broad spectral coverage, enhanced selectivity, and improved robustness for tissue characterization.
Tailored Layer Composition and Geometric Optimization	The multilayer absorber structure and geometric parameters are optimized to support controlled impedance matching over the operating band.	Improved impedance matching minimizes reflection losses and maximizes absorption efficiency.
Hybrid Resonator Coupling Scheme	Multiple resonant elements are coupled to generate spectral densification and mode hybridization.	Hybridized modes enhance near-field confinement and increase sensitivity to dielectric perturbations.
High Sensitivity	The proposed biosensor achieves a Euclidean sensitivity of 629.95 THz/RIU.	Strong field localization and broadband spectral separation enable accurate discrimination between healthy and cancerous tissue states.
High Figure of Merit	The sensor achieves a figure of merit of 15,179.585 RIU^{-1}.	The high FOM demonstrates excellent sensing resolution and dielectric differentiation capability.
High Quality Factor	The absorber exhibits an average quality factor of 61.566 across the dominant resonances.	Sharp resonances improve spectral selectivity and facilitate the detection of subtle dielectric variations associated with early-stage cancer.
Enhanced Electromagnetic Field Localization	Strong electric and magnetic field confinement occurs at resonant hotspots throughout the structure.	Localized field enhancement amplifies interactions with biological samples and improves sensing performance.

imaging. Incorporation of uncertainty metrics and explainable AI will further strengthen clinical reliability and regulatory acceptance.

Beyond NMSC, the proposed metamaterial approach may be generalized to other biological conditions characterized by dielectric heterogeneity, including breast tumors, precancerous cervical lesions, inflammatory tissue, or fibrotic disorders. The broadband nature of the device, combined with distributed resonance hotspots, makes it amenable to multi-analyte detection and opportunistic biomarker screening. Furthermore, by tailoring geometric symmetries or adding graphene, 2D materials, or tunable semiconductors, the device can evolve into an actively reconfigurable biosensor capable of dynamic frequency selection or analyte-specific spectral gating.

The integration of terahertz metamaterials, broadband diagnostics, and AI-assisted interpretation opens a path toward a new class of noninvasive clinical instrumentation. Continued progress in computational modeling, material fabrication, multimodal imaging, and data-driven inference will be crucial for translating the technology from laboratory settings to real-world dermatological practice.

11. Conclusions

This work presents a highly sensitive multiband terahertz metamaterial biosensor specifically engineered for early non-melanoma skin cancer detection. The device demonstrates a unique hybrid absorber architecture capable of generating approximately twenty resonance modes within the 0–5 THz band, with numerous peaks exceeding 95% absorptivity. Through careful geometric optimization and multilayer configuration, the sensor achieves simultaneous negative permittivity, negative permeability, and negative refractive index (double-negative response), producing strong near-field confinement and highly localized electromagnetic coupling with biological tissue.

The broadband design enables detection without dependence on a single resonance frequency, resulting in superior stability against spectral drift and environmental uncertainties. Quantitative analysis confirms the biosensor's exceptional performance, including a sensitivity of 629.95 THz/RIU, a quality factor exceeding 61, and a record figure of merit of 15,179.585 RIU^{-1}, surpassing previous metamaterial-based biosensors reported in literature. Field-based characterization further validates the resonance-localized mechanisms responsible for tissue discrimination.

To address diagnostic reliability, the sensing platform incorporates an AI-assisted spectral interpretation framework. By leveraging vectorized S-parameters, broadband absorption metrics, and pattern-based similarity measures, the AI model accurately differentiates healthy from cancerous tissue without invasive labeling. Complementary microwave imaging adds a spatial localization layer, enabling a multimodal diagnostic pipeline that unifies spectral sensing, image-based detection, and automated classification.

Collectively, these results demonstrate a compact, label-free, and non-invasive biosensing strategy capable of identifying subtle dielectric perturbations associated with early-stage non-melanoma skin cancer. The convergence of advanced metamaterial physics, broadband spectral engineering, and machine learning provides a pathway toward clinically viable diagnostic tools. Future work will extend the platform to experimental validation, hardware integration, and broader biomedical applications, establishing a foundation for next-generation terahertz diagnostic systems

12. Practical constraints and future directions for experimental realization

This study delineates the essential steps required to translate terahertz (THz) biosensing technologies from numerical design toward practical implementation in skin cancer diagnostics, with particular emphasis on experimental feasibility and clinical relevance. A primary objective of future work is the fabrication and experimental validation of the proposed THz metamaterial biosensor to confirm its numerically predicted sensitivity, bandwidth, and operational stability under realistic conditions. Following fabrication, systematic characterization using state-of-the-art THz measurement platforms will be necessary to accurately evaluate the spectral response, resonance fidelity, and robustness of the device.

As an intermediate and critical validation stage, tissue-equivalent phantoms with well-defined dielectric properties will be employed. These phantoms provide a controlled environment for investigating THz–matter interactions and enable fine-tuning of sensor parameters prior to biological testing, thereby reducing uncertainty and improving experimental reproducibility.

Progression toward clinically meaningful evaluation will require strict ethical and regulatory approvals for studies involving human-

derived samples. Upon approval, ex vivo measurements on excised skin tissues will be conducted to assess the biosensor's capability to reliably discriminate between malignant and healthy tissue. These investigations will be supported by comprehensive statistical analyses of diagnostic performance metrics, including sensitivity, specificity, and overall accuracy. Ultimately, controlled clinical studies will be essential to benchmark the proposed approach against established diagnostic modalities and to demonstrate compatibility with real-world clinical workflows.

Despite the promising numerical outcomes, the present work is inherently limited by the absence of experimental verification. This limitation arises primarily from the technical challenges associated with fabricating and characterizing micron-scale, multilayer metamaterial structures operating in the THz frequency range. Such experiments require advanced micro- and nanofabrication facilities, high-precision THz spectroscopy systems, and stringent control of biological sample conditions. Nevertheless, recent advances in high-resolution lithography, thin-film deposition, flexible electronics, and THz instrumentation indicate that these challenges are becoming increasingly surmountable.

The proposed biosensor design is grounded in experimentally reported dielectric contrasts between healthy and cancerous skin tissues (Liu et al., 2020; Saadeldin et al., 2019; Pickwell and Wallace, 2006; Berry et al., 2003; Rm, 2002; Wallace et al., 2004), with material parameters adopted from validated literature to ensure physical realism in the simulations. Comprehensive full-wave electromagnetic modeling was employed to assess absorption characteristics, sensitivity, quality factor, and figure of merit, revealing competitive or superior performance compared with existing THz biosensing platforms. Although experimental confirmation is still forthcoming, the strong theoretical and numerical foundation provides confidence in the anticipated diagnostic potential of the proposed sensor.

Beyond sensing performance, the planar metamaterial absorber architecture offers distinct advantages in terms of scalability, compactness, and potential suitability for future in vivo applications. Remaining challenges include mitigating THz attenuation in biological media, ensuring long-term biocompatibility, and integrating the sensor into portable and user-friendly diagnostic systems. Ongoing efforts are therefore focused on collaborative experimental validation using flexible, low-loss substrates and established THz imaging and spectroscopy protocols. Future research will further explore system miniaturization, adaptation to point-of-care diagnostic platforms, and extension of the proposed framework to other cancer types and biomedical sensing applications.

CRediT authorship contribution statement

Musa N. Hamza: Writing – review & editing, Writing – original draft, Resources, Methodology, Investigation, Formal analysis, Data curation, Conceptualization. **Mohammad Alibakhshikenari:** Writing – review & editing, Writing – original draft, Resources, Methodology, Investigation, Funding acquisition, Formal analysis, Data curation, Conceptualization. **Bal Virdee:** Writing – review & editing, Writing – original draft, Visualization, Resources, Methodology, Formal analysis, Data curation, Conceptualization. **Renu Karthick Rajaguru Jayanthi:** Writing – review & editing, Writing – original draft, Resources, Methodology, Formal analysis, Data curation, Conceptualization. **Sunil Lavadiya:** Writing – review & editing, Writing – original draft, Resources, Methodology, Formal analysis, Data curation, Conceptualization. **Iftikhar ud Din:** Writing – review & editing, Writing – original draft, Resources, Methodology, Investigation, Formal analysis, Data curation, Conceptualization. **Bruno Sanches:** Writing – review & editing, Writing – original draft, Resources, Methodology, Investigation, Formal analysis, Data curation, Conceptualization. **Slawomir Koziel:** Writing – review & editing, Writing – original draft, Resources, Methodology, Investigation, Funding acquisition, Formal analysis, Data curation, Conceptualization. **Abinash Panda:** Writing – review & editing, Writing – original draft, Resources, Methodology, Formal analysis, Data curation, Conceptualization. **Ali Farmani:** Writing – review & editing, Writing – original draft, Resources, Methodology, Formal analysis, Data curation, Conceptualization. **Zinelabiddine Mezache:** Writing – review & editing, Writing – original draft, Resources, Methodology, Formal analysis, Data curation, Conceptualization. **Zaid Ahmed Shamsan:** Writing – review & editing, Writing – original draft, Resources, Methodology, Formal analysis, Data curation, Conceptualization. **Hassan Zakeri:** Writing – review & editing, Writing – original draft, Resources, Methodology, Formal analysis, Data curation, Conceptualization. **Tran Huy Hung:** Writing – review & editing, Writing – original draft, Resources, Methodology, Formal analysis, Data curation, Conceptualization.

Funding

Co-funded by the European Union. Views and opinions expressed are however those of the author(s) only and do not necessarily reflect those of the European Union or the European Research Executive Agency. Neither the European Union nor the granting authority can be held responsible for them. Besides that, this publication has emanated from research jointly funded by Taighde Éireann – Research Ireland under Grant number 13/RC/2094_2, the European Union's Marie Sklodowska-Curie Actions under grant number 101126578 and was supported in part by University of Galway. Additionally, part of this research has been supported by the Icelandic Research Fund (Grant No. 2410297) and the National Science Centre of Poland (Grant No. 2022/47/B/ST7/00072).

Declaration of competing interest

The authors declare that they have no known competing financial interests or personal relationships that could have appeared to influence the work reported in this paper.

Data availability

No data was used for the research described in the article.

References

Abose, T.A., Assefa, B.G., Mekonen, Y.A., Gudeta, N.W., 2025. Spectral efficiency and BER analysis of RNN based hybrid precoding for cell free massive MIMO under terahertz communication. PloS One 20 (8), e0328499.

Asgari, S., Fabritius, T., 2023. Numerical simulation and equivalent circuit model of multi-band terahertz absorber composed of double-sided graphene comb resonator array. IEEE Access 11, 36052–36063.

Ahmed, S., Alam, T., Kirawanich, P., Singh, M.J., Islam, M.T., 01 September 2025. . Highly sensitive circle enclosed D-pad resonator-based narrowband metamaterial absorber for biosensing applications. IEEE Sensors J. 25 (17), 32536–32545.

Asgari, S., Granpayeh, N., Fabritius, T., 2020. Controllable terahertz cross-shaped three-dimensional graphene intrinsically chiral metastructure and its biosensing application. Opt. Commun. 474, 126080.

Azab, M.Y., Hameed, M.F.O., Nasr, A.M., Obayya, S., 2021. Highly sensitive metamaterial biosensor for cancer early detection. IEEE Sensors J. 21 (6), 7748–7755.

Bani, M.M., Mynuddin, M., Noor, K.S., Ferdous, A.I., Islam, M.S., 2025. Towards point-of-care HIV testing: terahertz PCF sensor integration and miniaturization. PLoS One 20 (7), e0327357.

Berry, E., et al., 2003. Optical properties of tissue measured using terahertz pulsed imaging. *Proceedings of SPIE: Medical Imaging* 2003: *Physics of Medical Imaging*. 5030, pp. 459–470.

Bhati, R., Malik, A.K., 2022. Ultra-efficient terahertz metamaterial sensor. Res. Optics 8, 100236.

Chen, T., Zhang, D., Huang, F., Li, Z., Hu, F., 2020. Design of a terahertz metamaterial sensor based on split ring resonator nested square ring resonator. Mater. Res. Express 7 (9), 095802.

Chen, Z., et al., 2023. Graphene multi-frequency broadband and ultra-broadband terahertz absorber based on surface plasmon resonance. Electronics 12 (12), 2655.

Elalaouy, O., Das, S., El Ghzaoui, M., Algarni, A.D., Madhav, B.T.P., Foshi, J., 2025. An ultra-thin polarization-sensitive quad-band metamaterial absorber (QMMA) with ten absorption peaks for diversified advanced millimeter-wave wireless applications. J. Electron. Mater. 1–20.

El-Wasif, Z., Ismail, T., Hamdy, O., 2023. Design and optimization of highly sensitive multi-band terahertz metamaterial biosensor for coronaviruses detection. Opt. Quant. Electron. 55 (7), 604.
Farooq, S., Habib, M., Saleem, M.F., Dahar, R.H., Cardozo, O., de Araujo, R.E., 2024. Advanced sensing applications utilizing a high-performance narrowband metamaterial perfect absorber based on ZnO architecture. IEEE Sensors J. 24 (15), 23968–23975.
Ferdous, A.I., et al., 2025. Pioneering terahertz blood analysis: hollow-core PCF with optimized sensitivity and low loss. PLoS One 20 (3), e0319860.
Fu, H., Chen, F., 2026. Dual-narrowband terahertz absorber with independently tunable amplitude and frequency: a theoretical study. Phys. Lett. A 574, 1–10.
Hamza, M.N., Islam, M.T., 2023. Designing an extremely tiny dual-band biosensor based on MTMs in the terahertz region as a perfect absorber for non-melanoma skin Cancer diagnostics. IEEE Access 11, 136770–136781.
Hamza, M.N., et al., April 2024. Designing a high-sensitivity microscale triple-band biosensor based on terahertz MTMs to provide a perfect absorber for non-melanoma skin Cancer diagnostic. IEEE Photonics J. 16 (2), 5900113.
Hamza, M.N., Islam, M.T., Lavadiya, S., Koziel, S., Ud Din, I., Sanches, B., 01 June 2024. Designing a high-sensitivity dual-band nano-biosensor based on petahertz MTMs to provide a perfect absorber for early-stage non-melanoma skin cancer diagnostic. IEEE Sens. J. 24 (11), 18418–18427.
Hamza, M.N., et al., 2025. Design of a high-sensitivity MTM-based multi-band micro-biosensor for early-stage non-melanoma skin cancer diagnosis in the terahertz region. Opt. Laser Technol. 192, 114015.
Han, W., et al., 15 April 2025. Selectable narrow-band anisotropic perfect absorbers based on α-MoO3 metamaterials for refractive index sensing. IEEE Sensors J. 25 (8), 13149–13159.
Hoque, A.M.T., Islam, A., Haider, F., Aoni, R.A., Ahmed, R., 2025. Point-of-care testing of hyponatremia and hypernatremia levels: an optoplasmonic biosensing approach. PloS One 20 (4), e0319559.
Hoseini, E., Mir, A., Farmani, A., 2022. Modeling and proposal of a black phosphorus-based nanostructure for detection of avian influenza virus in infrared region. Optical Quantum Electronics 54 (10), 609.
Hu, H., Qi, B., Zhao, Y., Zhang, X., Wang, Y., Huang, X., 2022. A graphene-based THz metasurface sensor with air-spaced structure. Front. Phys. 10, 990126.
Hu, H., Zhang, H., Jiang, H., Cui, Z., Wang, Y., Wu, D., 2025. Tunable multifunctional terahertz metamaterial device based on metal-dielectric-vanadium dioxide. Opt. Laser Technol. 181, 111629.
Jiang, H., Wang, B., Liu, Z., 2025. New dual-peak high-performance structure utilizing terahertz metamaterial metasurface for concentration detection of H2 and CH4 gases. Opt. Laser Technol. 186, 112728.
Kazemi, N., Abdolrazzaghi, M., Musilek, P., Baladi, E., 15 December 2024. A planar compact absorber for microwave sensing based on transmission-line metamaterials. IEEE Sensors J. 24 (24), 41864–41874.
Khalil, M.A., et al., 2025. A compact tri-octagonal negative indexmetamaterial sensor for liquid adulteration detection. Opt. Laser Technol. 184, 112499.
Khandakar, K., et al., 2025. Illegal drugs sensor: performance evaluation and identification based on terahertz photonic crystal fiber. PloS One 20 (6), e0327013.
Kundu, D., et al., 2025. Optimized PCF architectures for THz detection of aquatic pathogens: enhancing water quality monitoring. PloS One 20 (1), e0317533.
Lee, H.-N., Park, Y., Park, J.-T., Yang, J.-R., 2025. Signal preprocessing for foreign body detection using terahertz real-time non-destructive imaging system. PloS One 20 (6), e0319978.
Li, D., et al., 2021. Identification of early-stage cervical cancer tissue using metamaterial terahertz biosensor with two resonant absorption frequencies. IEEE J. Sel. Top. Quantum Electron. 27 (4), 1–7.
Li, B., et al., 2025a. Ultra-broadband and wide-angle metamaterial absorber based on vertical three-square patches structure gallium nitride for terahertz wave. J. Electron. Mater. 1–11.
Li, J., Chen, H., Yap, S.L., Zhang, B., 2025b. A temperature-insensitive graphene-water-based ultra-wideband terahertz metamaterials absorber designed using deep neural networks. Opt. Laser Technol. 185, 112591.
Liu, L., Liu, W., Song, Z., 2020. Ultra-broadband terahertz absorber based on a multilayer graphene metamaterial. J. Appl. Phys. 128 (9).
Liu, Y., et al., 2025. Temperature and refractive index THz sensor based on all-dielectric InSb metasurfaces: Y. Liu et al. J. Electron. Mater. 1–12.
Mezache, Z., Hafdi, Z., Tao, J., 2023. Design of a novel graphene buzzle metamaterial refractometer for sensing of cancerous cells in the terahertz regime. Optik 287, 171170.
Miah, A., Al Zafir, S., Hasnain, M., Das, J., Haque, S.M.A., Wahed, A., 2025. Triple-band highly sensitive terahertz metamaterial absorber for biomedical sensing applications. PloS One 20 (8), e0328077.
Naim, M.N.R., Upoma, J.T., Ferdous, A.I., Khandakar, K., Sadeque, M.G., Rana, M.S., 2025. Terahertz spectrum-based refractive index sensor for brain lesion detection using photonic crystal fibers. PloS One 20 (3), e0320355.
Nickpay, M.-R., Danaie, M., Shahzadi, A., 2021. Highly sensitive THz refractive index sensor based on folded split-ring metamaterial graphene resonators. Plasmonics 1–12.
Park, S., et al., 2014. Detection of microorganisms using terahertz metamaterials. Sci. Rep. 4 (1), 4988.
Park, S., Cha, S., Shin, G., Ahn, Y., 2017. Sensing viruses using terahertz nano-gap metamaterials. Biomed. Opt. Express 8 (8), 3551–3558.
Parvin, T., Ahmed, K., Alatwi, A.M., Rashed, A.N.Z., 2021. Differential optical absorption spectroscopy-based refractive index sensor for cancer cell detection. Opt. Rev. 28, 134–143.
Patel, S.K., Surve, J., Parmar, J., 2022. Detection of cancer with graphene metasurface-based highly efficient sensors. Diamond Relat. Mater. 129, 109367.
Pickwell, E., Wallace, V., 2006. Biomedical applications of terahertz technology. J. Phys. D Appl. Phys. 39 (17), R301.
Rm, W., 2002. Terahertz pulse imaging in reflection geometry of human skin cancer and skin tissue. Phys. Med. Biol. 47, 3853–3863.
Saadeldin, A.S., Hameed, M.F.O., Elkaramany, E.M., Obayya, S.S., 2019. Highly sensitive terahertz metamaterial sensor. IEEE Sensors J. 19 (18), 7993–7999.
Sadeque, M.G., et al., 2025. Hollow-core PCF for terahertz sensing: a new approach for ethanol and benzene detection. PloS One 20 (3), e0320805.
Sharma, P., Sharan, P., Deshmukh, P., 2015. A photonic crystal sensor for analysis and detection of cancer cells. *2015 International Conference on Pervasive Computing (ICPC)*. IEEE, pp. 1–5.
Sharma, S., Kumar, A., Saini, T.S., 2025. Design and simulation of a terahertz sensor for blood components detection using photonic crystal fiber: S. Sharma et al. J. Electron. Mater. 1–13.
Shen, Y., et al., 2023. Low-concentration biological sample detection using an asymmetric split resonator terahertz metamaterial. Photonics 10 (2), 111. MDPI.
Sun, H., et al., 15 August 2025. Terahertz perfect metasurface absorber based on groove-ring-shaped Ti 3 C 2 T x MXene for refractive index sensing application. IEEE Sensors J. 25 (16), 30845–30853.
Tan, C., et al., 2022. Cancer diagnosis using terahertz-graphene-metasurface-based biosensor with dual-resonance response. Nanomaterials (Basel, Switzerland) 12 (21), 3889.
Teber, A., 2024. A dual-band terahertz metamaterial absorber using an all-metal aluminum hexagonal metasurface structure for sensing of cancerous cells. J. Electronic Materials 53 (5), 2686–2701.
Tong, Y., et al., 2025. Design and analysis of terahertz wave all-dielectric grating magnetic reflector. J. Electron. Mater. 1–11.
Uddin, M.K., et al., 2025. Polarization insensitive U-coupled splits ring resonator-based hexa-band metamaterial absorber for concentration of solid material sensing applications. Opt. Laser Technol. 181, 111975.
Vafapour, Z., Troy, W., Rashidi, A., 2021. Colon cancer detection by designing and analytical evaluation of a water-based THz metamaterial perfect absorber. IEEE Sensors J. 21 (17), 19307–19313.
Vineetha, K., Kumar, M. Siva, Rao, B.S.S., Kumar, O.P., S. R., V., Madhav, B., 2025. Design and implementation of a graphene–polyimide-based H-slot terahertz antenna for wireless and biomedical applications. PLoS One 20 (12), e0336921.
Wallace, V.P., et al., 2004. Terahertz pulsed imaging of basal cell carcinoma ex vivo and in vivo. Br. J. Dermatol. 151 (2), 424–432.
Wang, B.-X., He, Y., Lou, P., Xing, W., 2020. Design of a dual-band terahertz metamaterial absorber using two identical square patches for sensing application. Nanoscale Adv. 2 (2), 763–769.
Wang, Y., et al., 2021. Terahertz tunable three band narrowband perfect absorber based on Dirac semimetal. Physica E 131, 114750.
Wang, W., Wu, Q., Li, H., Li, M., 2025a. Numerical research on terahertz hyperbolic metamaterials composed of interlaced graphene-dielectric multilayers and a microcavity. Opt. Laser Technol. 181, 111793.
Wang, W., Li, G., Yang, G., Schubert, D.W., 2025b. Enhanced multifunctionality of carbon black-modified melamine sponge: flame retardancy, electromagnetic wave absorption, and sensing capabilities. J Electronic Materials 54 (3), 2111–2121.
Wekalao, J., et al., 2025. Enhanced surface plasmon resonance biosensor with graphene-black phosphorus heterostructure for ultra-high sensitivity refractive index detection with machine learning for behaviour prediction. PloS One 20 (11), e0332356.
Yang, J., Lin, Y.-S., 2021. Design of tunable terahertz metamaterial sensor with single- and dual-resonance characteristic. Nanomaterials 11 (9), 2212.
Yang, Q., et al., 2026. Broadband perfect absorber based on graphene-silicon Mie heterojunctions for cancer cell detection. Physica E 177, 1–9.
Yin, S., Zhong, H., Huang, W., Zhang, W., 2025. Deep learning enabled design of terahertz high-Q metamaterials. Opt. Laser Technol. 181, 111684.
Zhang, J., et al., 15 December 2024. Design of pixel terahertz metamaterial absorber sensor based on an improved ant colony algorithm. IEEE Sensors J. 24 (24), 40801–40810.
Zhang, X., Wang, Z., Gong, Y., 2025. Progress in multifunctional tunable terahertz metasurface waveplates. J. Electron. Mater. 1–22.
Zheng, Y., Chen, Y., Xu, Y., 2024. Toroidal dipole all-dielectric Metasurfaces with high sensitivity, high figure of merit, and robustness for refractive index sensing. J. Electronic Materials 53 (2), 674–682.
Zhuang, S., et al., 2022. Graphene-based absorption–transmission multi-functional tunable THz metamaterials. Micromachines 13 (8), 1239.



Musa N. Hamza received the B.Sc. degree from the Department of Physics, Faculty of Science and Health, Koya University, Koysinjaq, Erbil, Iraqi Kurdistan, Iraq, in 2015, and the M.Sc. degree from the Department of Medical Physics, College of Medical and Applied Sciences, Charmo University, Chamchamal, Sulaymaniyah, in 2023. His research interests include medical physics, the diagnosis of different types of cancer at an early stage, antenna arrays, metamaterials, sensors, and biosensors.



Mohammad Alibakhshikenari (Member, IEEE) was born in Mazandaran, Iran, in February 1988. He received the Ph.D. degree with the European label and Excellent Cum Laude in electronics engineering from the University of Rome "Tor Vergata'' (UNITOV), Italy, in February 2020. From May 2018 to December 2018, he was a Ph.D. Visiting Researcher with the Chalmers University of Technology, Gothenburg, Sweden. His training during this visit included a research stage at Swedish Company "Gap Waves AB." During his Ph.D. (Nov. 2016 – Feb. 2020), he was recognized as the winner of 13 grants for attending the Doctoral Schools organized by ESoA (European School of Antennas, 5), EUPROMETA (European Doctoral Programmes in Metamaterials, 3), EuMC (European Microwave Conference, 2), SIE (Società Italiana di Elettronica - Italian Society of Electronics, 1), ITMO University (Nanophotonics and Metamaterials, 1), Aix-Marseille Université (Metamaterials, 1), which were held in various European universities. He successfully achieved all 30 credits provided by Doctoral Schools leading him to obtain his Ph.D. degree with European label.

He is now a Marie Sklodowska-Curie, ROSETTA (Responsible Time and Tech in an Accelerated Digitised World), and LERO (the Research Ireland Centre for Software) Postdoctoral Fellow at the University of Galway, Ireland. As part of this fellowship, he had five research visits at the Microwave Engineering Center for Space Applications (MECSA, October 2025); Universitat Ramon Llull, Barcelona, Spain (October 2025); Institute of Science Tokyo, Japan (November 2025); Pusan National University, Busan, South Korea (December 2025); and Sogang University, Seoul, South Korea (December 2025).

From September 2024 to June 2025, he was with UNITOV as a Senior Researcher. From July 2021 to August 2024, he was with the Department of Signal Theory and Communications, Universidad Carlos III de Madrid (uc3m), Spain, as a Marie Sklodowska-Curie and CONEX-Plus Fellow. During this Program he has spent two secondments at the: 1) Microwave Engineering Center for Space Applications (MECSA), Rome, Italy, from April to August 2024, and 2) SARAS Technology Ltd., Company, Leeds, U.K., from December 2022 to May 2023. In addition, during this program he had one-week research visits at the: 1) University of Catania, Italy, in May 2024, along with an invited lecture entitled "Terahertz Antennas based on Metasurface and SIW'' for the master's and Ph.D. students, and postdoctoral researchers; 2) University of Messina, Italy, in May 2024; 3) University of Bradford, U.K., in May 2023; and 4) Edinburgh Napier University, U.K., in April 2023.

In 12th May 2026, he received a letter of acknowledgement from President of the University of Galway, "Prof. David Burn", and he was commended due to his contribution to the research excellence of the university. In academic year 2021/2022, he received the letter of acknowledgement from the Vice-Rector of studies of the Universidad Carlos III de Madrid, "Prof. Marta Pilar Macias Dorissa", due to his contribution to the teaching excellence in the "Electromagnetic Fields". In November 2019, he was winner of a postdoctoral research fund for two years awarded by UNITOV. His research interests include "Electromagnetic fields, antennas and wave-propagations, metamaterials and metasurfaces, RF/microwave systems, sensors, next generation of wireless communications, multiple input multiple output (MIMO) systems, millimeter-waves and terahertz devices, and beamforming networks". His research activities are documented in about 200 papers published in international journals, 2 books, 10 book chapters, and about 116 papers in proceedings of international conferences including 50 in-person presentations in 32 conferences and 27 on-line presentations in 13 conferences (the rest were presented by his colleagues). His research works received more than 10K citations with H-index above 60 reported by Scopus, Google Scholar, and ResearchGate. According to Stanford University yearly analysis, he has been among the World's Top 2% Scientists of highly cited scientific authors, since 2020. He was listed in both Career Long and Single Year Impact in Stanford's list. He was a recipient of two young engineer awards of the 47th and 48th European Microwave Conferences held in Nuremberg, Germany, in 2017, and in Madrid, Spain, in 2018, respectively. In April 2020, his research article entitled "High-Gain Metasurface in Polyimide On-Chip Antenna Based on CRLH-TL for Sub Terahertz Integrated Circuits, published in Scientific Reports, volume 10, Article number 4298 (2020)'' was awarded as the Best Month Paper at the University of Bradford, U.K. In addition, he serves the role of an Associate Editor for two scientific journals of Radio Science and The Journal of Engineering (IET). He acts as a referee in several journals, and the technical program committee (TPC) and session chair of several international conferences. In addition, he is member of the international reviewer panel of Dutch Research Council (NWO); U.K. Research and Innovation (UKRI) Funding Service; National Natural Science Foundation of China (NSFC) / Research Grants Council (RGC) of Hong Kong; IEEE MTT-S Education Committee Fellowships and Scholarships; and the External Examiner of several Ph.D. dissertations from various worldwide universities.



Bal S. Virdee (SM'08) received the B.Sc. and MPhil degrees in Communications Engineering from the University of Leeds, UK, and his Ph.D. in Electronic Engineering from the University of London, UK. He has worked in industry for various companies including Philips (UK) as an R&D-engineer and Teledyne Defence and Space as a future products developer in RF/microwave communications. He has taught at several academic institutions before joining London Metropolitan University where he is a Senior Professor of Communications Technology in the School of Computing and Digital Media where he is Head the Communications Technology Research Center. His research, in collaboration with industry and academia, is in wireless communications encompassing mobile-phones to satellite-technology. Prof. Virdee has chaired technical sessions at IEEE international conferences and published numerous research papers. He is Executive Member of IET's Technical and Professional Network Committee on RF/Microwave-Technology. He is a Fellow of IET and a Senior-Member of IEEE.



Renu Karthick Rajaguru Jayanthi was born in India. He obtained his master degree in robotics at the University of Bristol, UK. He is now a PhD candidate in electronics, more specifically, biosensors at the London Metropolitan University, UK.



Sunil Lavadiya working as Associate Professor in the Department of Information and Communication Technology at Marwadi University, Rajkot, Gujarat. He has completed his PhD on the topic of High Gain Frequency Reconfigurable Liquid Metamaterial Microstrip Patch Antenna. He has completed an M. Tech in communication engineering from Nirma University in 2010, and a B.Tech in Electronics and Communication from Saurashtra University in 2008. He has adapted to all aspects of Electronics and Communication Engineering, including training, education, and research. He works in the MIMO, Sensors, Reconfigurable, Superstrate, Solar absorber and liquid antennas. He is a member of professional bodies like IEEE and IETE. He has published 50 SCI research articles, 12 SCOPUS index articles, 8 book chapters, and 5 papers in an international conference and filed four design patents and one copyright.



Iftikhar ud din Received B.Sc. and M.Sc. Degree in Telecommunication Engineering from University of Engineering and Technology, Peshawar, Pakistan, in 2017 and 2021 respectively. He is the member of the Antennas & Microwave Engineering Research Group (AMERG) in UET Mardan. His current research interests include UWB antennas, FSS based UWB antennas and Sub-6 GHz 5G antennas, 5G millimeter wave antennas and MIMO antennas, frequency selective surfaces, EBGs and Metamaterial based antenna.



Bruno Cavalcante de Souza Sanches received the B.S. degree in information engineering and the M.Sc. degree in energy from the Federal University of ABC, Santo André, Brazil. He received the Ph.D. degree in microelectronics with the Integrated Systems Laboratory (LSI), University of São Paulo, São Paulo, Brazil, working in the design of a novel mixed signal integrated circuit used in the ALICE experiment in the CERN LHC. Bruno has more than fifteen years of experience in electronics and microelectronics design. He has been involved in hardware development, smart grids, algorithms, artificial intelligence, digital communication systems, EDA tools, electronics for high energy physics experiments and in several systems targeting early cancer detection including bioimpedance spectroscopy and microwave imaging.



Slawomir Koziel received the M.Sc. and Ph.D. degrees in electronic engineering from Gdansk University of Technology, Poland, in 1995 and 2000, respectively. He also received the M. Sc. degrees in theoretical physics and in mathematics, in 2000 and 2002, respectively, as well as the PhD in mathematics in 2003, from the University of Gdansk, Poland. He is currently a Professor with the Department of Engineering, Reykjavik University, Iceland. His research interests include CAD and modeling of microwave and antenna structures, simulation-driven design, surrogate-based optimization, space mapping, circuit theory, analog signal processing, evolutionary computation and numerical analysis.



Abinash Panda (Senior Member, IEEE) received the B.Tech. and M.Tech. degrees in Electronics and Communication Engineering from Biju Patnaik University of Technology (BPUT), Odisha, India, and the Ph.D. degree from the National Institute of Technology Silchar, Assam, India. He subsequently worked as a Visiting Researcher at Slovak University of Technology Bratislava, Slovakia.and Postdoctoral Researcher at Chulalongkorn University, Bangkok, Thailand. He is currently working as Associate Professor in the department of Electronics and Communication Engineering at CMR Institute of Technology (CMRIT), Bengaluru, India. His research interests include photonic waveguides, photonic crystals, fiber and integrated photonics, bio-photonic and plasmonic sensors, optoelectronic devices, MEMS, and nanomaterial synthesis and characterization. His recent work focuses on 2D material-assisted SPR biosensors, advanced optical sensing platforms, and photonic device design for biomedical and environmental applications. He has published several research articles in reputed journals and conferences and is actively involved in IEEE activities, student mentoring, and interdisciplinary research collaborations.



Ali Farmani (Member, IEEE) received the B.Sc. degree in electrical engineering from the Shiraz University of Technology in 2008, the M.Sc. degree in electrical engineering from the University of Tabriz in 2010, and the Ph.D. degree in electrical engineering from Shiraz University in 2017. During his stay at Lorestan University as an Assistant Professor (2018–2024), he has mentored several B.Sc., ten M.Sc. theses, and four Ph.D. dissertations. He is the author of more than 106 ISI papers and three book chapters. His research interests are VLSI, nanoelectronics, plasmonics, and investigation of new materials for integrated photonics. He was a recipient of the fellowship for Ph.D. study at Shiraz University as an Exceptional Talent. He received the Shiraz Distinguished Ph.D. Dissertation Award for his work on plasmonic nanostructures. He was also a recipient of the Excellent Reviewer Award from Elsevier and IEEE Journals (2017–2024).



Zinelabiddine Mezache received the M.Sc. degree in optics, image, and vision (OIV) from Jean Monnet University, Saint-Étienne, France, in 2012, the M.Sc. degree in microelectronics, and the Ph.D. degree in nanotechnologies from the University of Constantine 1, Constantine, Algeria, in 2016. He has been a Full Professor at the Institute of Optics and Precision Mechanics, University of Ferhat Abbas Sétif 1, Sétif, Algeria, since 2017.



Zaid Ahmed Shamsan was a Postdoctoral Research Fellow with the Wireless Communication Center (WCC), Faculty of Electrical Engineering, Universiti Teknologi Malaysia (UTM), Malaysia, (April 2010-April 2012). He obtained his PhD and Master from Universiti Teknologi Malaysia (UTM), Malaysia, in Electrical, Electronics, and Telecommunications Engineering in 2010 and 2007, respectively. Shamsan received the B.Sc. (Hons.) degree in electronics and communication engineering from the Sudan University of Sciences and Technology (SUST), in 2002 (the 1st position in the class). From Nov. 2003 to Dec. 2005, Shamsan has worked as a reader in the Faculty of Engineering and Information Technology, Taiz University, Yemen. From Jul. 2007 to Feb. 2010, Dr. Shamsan was an assistant researcher at WCC focusing on several research projects mainly in the field of frequency spectrum management funded by the Malaysian Communications and Multimedia Commission (MCMC), which is successfully completed in 2010. He received a Bronze Medal in Geneva Innovation 2021 for his project RFID Lock Security Mechanism. He has successfully completed many research projects as Principal Investigator (PI) and Co-PI, funded by various research agencies and institutions in Malaysia and Saudi Arabia. He is currently a Professor with the Department of Electrical Engineering, College of Engineering, Imam Mohammad Ibn Saud Islamic University (IMSIU), Riyadh, Saudi Arabia. From 2012 to 2021, Prof Shamsan worked as a member of the international publishing unit (IPU) at the Deanship of Academic Research, IMSIU, and since 2021 he becomes the head of the IPU unit. In addition, He works as a consultant for the Deanship of Academic Research, IMSIU. He is interested in teaching courses, such as electrical circuits analysis, wireless mobile communication, wireless mobile networks, digital communication, satellite communication, communication electronics, and digital signal processing. Prof. Shamsan translated the book of "MIMO-OFDM Wireless Communications with Matlab by YS Cho et al." into Arabic language. He has published several scientific papers in high-impact factor and archival technical journals and conferences. His research interests include LTE-Advanced systems (4G), 5G and 6G Systems, orthogonal frequency-division multiplexing technology (OFDM), LMDS system analysis, interference analysis techniques, mathematical modeling for coexistence analysis in wireless networks, wave propagation propagation channel prediction and antenna, rainfall and dust storm analysis and mitigation, free space optics, and optical communication.



Hassan Zakeri was born in Rome, Italy, in 1996. He obtained the M.Sc. degree (Hons.) in Electrical Engineering from Amirkabir University of Technology (Tehran Polytechnic) in 2021. He is currently pursuing a Ph.D. in the Electromagnetic Research Laboratory of the Electrical Engineering Department at Amirkabir University of Technology. His research interests include Microwave Photonic, Antennas, terahertz devices and applications, optical fiber, 5G/6G and beyond wireless communications, and multipleinput multiple-output (MIMO) systems.



Tran Huy Hung earned his Bachelor's degree in Electronics and Telecommunications from Hanoi University of Science and Technology in 2013, followed by a Master's degree in Electronics – Computer Engineering from Ajou University, South Korea, in 2015. In 2020, he successfully defended his Ph.D. dissertation in Electrical and Electronics Engineering at Dongguk University, South Korea. Since July 2020, Dr. Hung has been a faculty member in the Department of Electrical and Electronics Engineering at Phenikaa University. His research areas include Reconfigurable antennas, Wideband antennas, Antennas for mobile devices, MIMO antennas.